

# Experiments on sub-tomographic imaging of a transparent birefringent phase pattern localized in a phase space

**SHEENAM SAXENA**

*A dissertation submitted for the partial fulfillment of  
the degree of Doctor of Philosophy*



Department of Physical Sciences  
Indian Institute of Science Education and Research Mohali  
Knowledge City, Sector 81, SAS Nagar, Manauli PO, Mohali 140306,  
Punjab, India.

August 2023



# Declaration

I hereby declare that the experiments of sub-tomographic imaging of a transparent birefringent phase pattern localized in a phase space in this thesis are partially carried out by me under the supervision of Dr. Mandip Singh at Indian Institute of Science Education and Research, Mohali. This work has not been submitted in any partial or full degree/ diploma/ fellowship to any institute or university.

**Sheenam Saxena**  
(Candidate)

I certify that the above statement made by the candidate are true to the best of my knowledge.

**Dr. Mandip Singh**  
(Supervisor)  
Associate Professor of Physics  
Department of Physical Sciences  
IISER Mohali



# Acknowledgment

The successful completion of this thesis has been made possible by the unwavering support and encouragement of numerous people, including my well-wishers, my friends, colleagues and various persons from this institution. At the end of my thesis, it is a pleasant task to express my gratitude to all those who contributed in many ways to the successful accomplishment of this study and made it an important milestone in the path of success in my life.

At this moment of accomplishment, I express my sincerest thanks to my revered supervisor Dr. Mandip Singh, Associate Professor of Physics for his keen interest, expert guidance and untiring efforts throughout my research work. I have been very fortunate to work with such a fine physicist with creativity, strong dedication and enormous physics knowledge. I owe a great deal of appreciation and gratitude to the worthy members of my advisory committee, Dr. Anosh Joseph and Dr. Satyajit Jena, who always supported me generously and gave constructive suggestions in my progress report presentations, thereby providing a smooth basis to overcome many difficulties that came in the path of completion of my work. I am also grateful to Prof. Arvind and Dr. Sanjeev Kumar for all the support they have given during and after the course work.

Fortunately, here I got a chance to gratefully acknowledge the unflagging support of some special friends on this campus - Arpita, Komal, Shaina, Shubahshree, Shushma and Vaishali. All of them pushed me and motivated me during my hard moments and were always there to lend a shoulder of support whenever I felt lost and dazed. Some special friends - Anjali, Aswathy, Jasleen, Pooja, Roohi, Sarika, Shilpa and Shivani were always there to remind me of life's true priorities during the inevitable ups and downs of my life. This would be the best possible way of making them realize that they were the hopes when my life was low and they were the places when I had nowhere to go. Life would have been way too different without you. Thankshhh..

I am also thankful to my Labmates and Batchmates. There are so many others whom I may have inadvertently left out and I sincerely thank all of them for their help.

# Abstract

In conventional imaging experiments, optically responsive objects localized in position space are imaged using a lens and hence viewed by the human eye. Recently, a counter intuitive concept and experiment on a three-dimensional tomographic imaging of a pattern localized in a phase space of atoms has been introduced in a paper entitled "Three-dimensional classical imaging of a pattern localized in a phase space, Phys. Rev. A 98, 053828" [1]. In experiment of Ref [1], objects imaged were three  $2D$  transparent masks. The experiment was based on the concept of velocity-selective hole-burning in the Doppler broadened absorption profile of an atomic gaseous medium. The object laser beam interacted with the objects and imprinted their tomographic images onto the phase space of an atomic medium. These patterns in phase space were localized in unique  $3D$  subspace of  $6D$  phase space spanned by  $\hat{x}$ ,  $\hat{y}$  and  $\hat{p}_z$  coordinates. These tomographic images in phase space were then captured by image laser beam. By varying the frequency of image laser beam, tomographic images at different locations on momentum axis were captured. However, method employed in this experiment can imprint and image only light absorbing objects. The work in this thesis presents an experiments to imprint a transparent birefringent phase pattern onto a phase space of an atomic gaseous medium. A position space localized  $2D$  transparent birefringent phase pattern is produced with a spatial light modulator (SLM). This position space localized pattern is imprinted onto the phase space of rubidium atoms at room temperature by using atomic state dependent velocity selective hole burning. The phase space localized transparent pattern is imaged by measuring the atomic state population difference induced phase shift at different detunings. Sub-tomographic images of the transparent phase space localized pattern obtained in this experiment are inverted with respect to each other. This transparent birefringent phase pattern donot absorb light but exhibit polarization dependent phase shift of the transmitted light. Therefore, these alphabets can modify the polarization of the transmitted light without absorption. The idea and technique reported in this thesis are inspired by the imprinting and tomographic imaging of such transparent birefringent phase pattern.



# Contents

<b>Declaration</b>	<b>i</b>
<b>Acknowledgment</b>	<b>iii</b>
<b>Abstract</b>	<b>v</b>
<b>List of Figures</b>	<b>ix</b>
<b>1 Introduction</b>	<b>1</b>
1.1 Historical Overview of Saturated Absorption Spectroscopy . . . . .	1
1.2 Historical Overview of Polarization Spectroscopy . . . . .	4
1.3 Brief History of Imaging Experiments . . . . .	6
1.3.1 Imaging of a Transparent Object . . . . .	6
1.3.2 Imaging of Bose Einstein Condensate . . . . .	8
1.3.3 Imaging in Position Space . . . . .	10
1.4 Thesis Outline . . . . .	12
<b>2 Atomic Structure of Rubidium</b>	<b>17</b>
2.1 Introduction . . . . .	17
2.2 Fine structure . . . . .	18
2.3 Hyperfine structure . . . . .	19
2.3.1 Magnetic Dipole Interaction . . . . .	19
2.3.2 Electric Quadrupole Hyperfine Interaction . . . . .	21
2.4 Rubidium Atoms . . . . .	22
2.5 Doppler Broadening . . . . .	24
2.6 Saturation Absorption Spectroscopy . . . . .	26
2.6.1 Theory . . . . .	27
2.6.2 Experimental Setup . . . . .	29

2.7	Polarization Doppler Free Spectroscopy . . . . .	33
2.7.1	Theory . . . . .	33
2.7.2	Experimental Setup . . . . .	38
2.8	Conclusion . . . . .	41
<b>3</b>	<b>3D Tomographic Imaging in Phase Space</b>	<b>43</b>
3.1	Introduction . . . . .	43
3.2	Velocity Selective Hole Burning . . . . .	43
3.3	Phase Space Imaging Based on Velocity Selective Hole-Burning . . . . .	46
3.3.1	Theory . . . . .	46
3.3.2	Experimental Setup . . . . .	49
3.4	Conclusion . . . . .	54
<b>4</b>	<b>Sub tomographic imaging of a birefringent phase pattern localized in a phase space</b>	<b>55</b>
4.1	Introduction . . . . .	55
4.2	Transparent Birefringent Phase Pattern Localized in a Position Space . . .	56
4.3	Imprinting of a Transparent Birefringent Phase Pattern onto a 3D Phase Space . . . . .	57
4.4	Imaging of a 3D Phase Space Localized Pattern . . . . .	61
4.5	Experimental Method and Results . . . . .	64
4.6	Conclusion . . . . .	68
<b>5</b>	<b>Conclusion</b>	<b>71</b>
	<b>Bibliography</b>	<b>73</b>

# List of Figures

1.1	Basic experimental setup for saturation absorption spectroscopy . . . . .	3
1.2	Experimental scheme of laser polarization spectrometer [2] . . . . .	5
2.1	Fine structure of $^{87}\text{Rb}$ due to spin-orbit coupling . . . . .	22
2.2	Hyperfine splitting of energy levels in $^{87}\text{Rb}$ . . . . .	23
2.3	Hyperfine splitting of energy levels in $^{85}\text{Rb}$ . . . . .	24
2.4	Experimental setup for Saturated Absorption Spectroscopy: Beam Splitter (BS); Mirror (M); Photodiode ( $D_1$ and $D_2$ ) . . . . .	27
2.5	Doppler broadened spectral lines for $^{87}\text{Rb}$ and $^{85}\text{Rb}$ . . . . .	28
2.6	Doppler broadened lines with dips representing hyperfine structure of $^{87}\text{Rb}$ and $^{85}\text{Rb}$ . . . . .	29
2.7	Saturated absorption lines . . . . .	30
2.8	$F_g = 2 \rightarrow F_e = 1, 2, 3$ transitions for $^{87}\text{Rb}$ . . . . .	31
2.9	Transitions induced by $\sigma^+$ pump beam. . . . .	34
2.10	Transitions induced by $\sigma^-$ pump beam. . . . .	35
2.11	Experimental setup for polarization doppler free spectroscopy: Polarization Beam Splitter (PBS); Mirror (M); Photodiode ( $D_1$ and $D_2$ ) ; Quarter wave plate ( $\lambda/4$ ); Half wave plate ( $\lambda/2$ ) . . . . .	36
2.12	Polarization spectra for $F_g = 2 \rightarrow F_e = 1, 2, 3$ transitions in $^{87}\text{Rb}$ . . . . .	37
2.13	Polarization spectra for $F_g = 2 \rightarrow F_e = 1, 2, 3$ transitions in $^{87}\text{Rb}$ . In this experiment, the circular polarization of the pump beam is opposite to the polarization of the pump beam considered in the experiment of Figure 2.12. By changing the circular polarization, the slope of the polarization signal has reversed. . . . .	40
3.1	A pattern localized in a $3D$ phase space and its three tomograms [1]. . . . .	48
3.2	Experimental schematic diagram [1] . . . . .	49

3.3	(a) A 2D transverse intensity profile of the overlapped object laser beams. All three letters overlap with each other [1]. (b) Transmittance, for the imaging laser beam, of the atomic medium in the presence of object laser beams without masks [1]. . . . .	50
3.4	Three tomographic images of a localized pattern in the 3D phase space captured at different detunings of the imaging laser beam. Each image is a plot of a change in the optical density $\Delta OD(z, y, \delta\nu)$ [1]. . . . .	52
3.5	(a) A photograph of overlapping neutral density filters [1]. An image, $\Delta OD(z, y, \delta\nu = 0)$ , of an area enclosed by a square as shown in (b) [1]. . .	53
4.1	A position space localized transparent birefringent phase pattern, $\phi(x, z)$ . .	57
4.2	(a) A position space localized transparent birefringent phase pattern $\phi(x, z)$ . (b) A transverse intensity profile of the retro-reflected beam measured by a camera-2 . . . . .	59
4.3	(a) Experimental schematic diagram of a sub-tomographic imaging experiment (b) part of the experiment to measure frequency difference of lasers by time domain interference on a fast response photodetector . . . . .	60
4.4	Experimental setup of a sub-tomographic imaging experiment . . . . .	62
4.5	(a) Transmittance of atomic medium when both laser beams are linearly polarized. (b) Photodetector $D_1$ output voltage when imprinting laser beam is $\hat{\sigma}^+$ polarized. (c) when imprinting laser beam is $\hat{\sigma}^-$ polarized. Dotted line represents the same plot without imprinting laser beam. Imaging laser beam is linearly polarized in all plots. . . . .	66
4.6	Two sub-tomographs of a 3D phase space localized pattern. Each plot is an experimentally constructed image, $p(x, y, \delta\nu) = -\ln\left(\frac{I_r(x, y, \delta\nu)}{I_i(x, y, \delta\nu)}\right)$ . (a) For $\delta\nu = -11.4$ MHz. (b) An inverted image for $\delta\nu = +8.6$ MHz. . . . .	67

# Chapter 1

## Introduction

### 1.1 Historical Overview of Saturated Absorption Spectroscopy

Saturated absorption spectroscopy has become an essential part of numerous experiments in atomic physics and associated fields since Bennet [3] and Lamb's [4] demonstration of spectral hole burning and saturated absorption with lasers. It has been employed for the investigation of atomic and molecular structure [5] as well as its use as a frequency reference [6]. The experimental application of the intrinsic narrow linewidths [7] in the helium-neon optical maser is restricted by the attainable frequency stabilization. The research undertaken by Bennett *et al* suggested a method to obtain an extremely high degree of relative frequency stability. They constructed a He-Ne maser having different mechanical design from the original He-Ne maser [8]. In his discussion of maser action Benett has made use of the notion of hole burning [3]. Lamb *et al* considered a theoretical model for the understanding of an optical maser. The medium consisted of thermally moving atoms interacting with electromagnetic field described classically. Depending on its trajectory, atoms see optical frequencies that have been Doppler shifted. There is very little overlapping between the two oscillations driven by two group of atoms moving at different velocities. The medium acquired non linear electric dipole moments under the action of the field. They also provided a more approximate discussion of maser action utilizing rate equations based on the concept of hole-burning [4].

Linear spectroscopy is a term used to describe the light-matter interaction with one primary incident radiation field which is weak and can be treated as a linear response

between the incident light and the matter. It is frequently envisioned as a "one photon in/one photon out" measurement when viewing the light field from a quantum mechanical perspective. Non linear spectroscopy is used to refer to a situation that deviates from this perspective; examples include observing how matter reacts to interactions with two or more distinct incident fields and situations in which the linear response theory is insufficient to explain how the material behaves, such as when extremely intense incident radiation is present. The core of saturation absorption spectroscopy is the non-linear interaction of an atom based on third order non-linearity. In addition to being fundamental to gas lasers [4, 9, 10], this non-linear spectroscopy is also important for laser cooling and trapping [11–13] and to many experiments in atom optics.

For example, resolution in optical spectroscopy of gases for a long time has been restricted by the Doppler effect, which imparts to each resonant line a relative width. The saturated-absorption technique [6] can bring a substantial improvement in this regard. By considering the nonlinear interaction of an atomic system with strong electromagnetic waves, one can substantially address only those atoms or molecules which have a zero axial velocity. The gaseous sample's absorption spectrum then consists of a line that has been Doppler broadened with a little dip in the middle. This dip, which closely resembles the Lamb dip seen on the output of gas lasers as the frequency is tuned in the cavity over the emission line, is orders of magnitude smaller than the Doppler width. This method is already being employed in spectroscopy [14, 15] and for laser frequency stabilization purposes [16]. To explain the formation of the dip, the already described hole-burning model [3] has been used. Such a dip in the absorption spectrum or a transmission peak occurs when two counterrunning laser beams are allowed to propagate in the cell containing gaseous atoms as shown in Figure 1.1. If we consider atoms with velocity  $\vec{v}$ , the two waves having frequency  $\omega$  in the laboratory frame will happen to have two different frequencies  $\omega_+ = \omega - \vec{k} \cdot \vec{v}$  and  $\omega_- = \omega + \vec{k} \cdot \vec{v}$ , where  $\vec{k}$  is the wave vector ( $|\vec{k}| = \omega/c$ ). The transparency of the atomic medium to the second beam (probe laser beam) is not affected by the first beam (pump laser beam) unless the two frequencies coincide in the atomic frame, that is when  $\vec{k} \cdot \vec{v} = 0$  (atoms with zero axial velocity). The hole-burning (or rate-equations) model suggests that one of the oppositely traveling waves (pump beam) saturates the group of atoms which have the right axial velocity which causes an increase in the transparency of the medium relative to the second wave (probe wave).

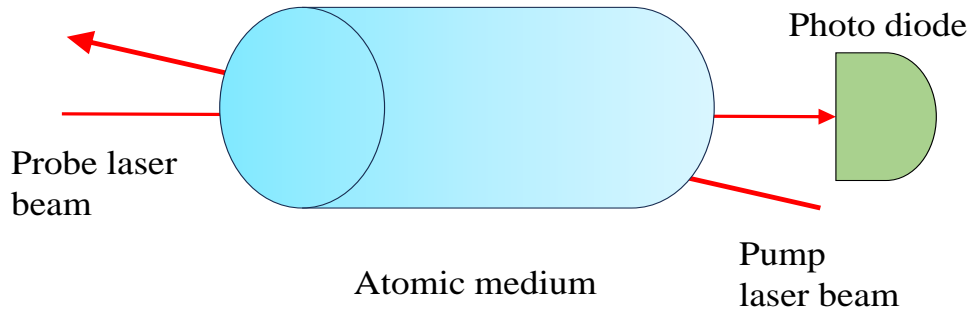


**Figure 1.1:** Basic experimental setup for saturation absorption spectroscopy

Haroche *et al* constructed a theory of the saturated-absorption in a two-level atomic system. The absorbing medium in this theory is exposed to irradiation by a quasi-running wave composed of a strong pump beam and a weak probe beam traversing in opposite direction. Some new findings not suggested by the so-called hole-burning or rate equation model are realized. Although the transmission peak is properly predicted by the hole burning model, the explanation above is merely qualitative since it only addresses population fluctuations and ignores the fact that atomic dipoles that absorb one wave are coherently driven by another. They proposed that nonlinear phenomena like Raman or multiphoton processes which are neglected in hole-burning model might potentially happen when two waves couple with the atomic system simultaneously. They discovered that the form of the probe-field-transmission peak line is significantly different from what is predicted by the rate equations. [17].

The  $D1$  and  $D2$  transitions are frequently studied in atomic physics:  $D2$  transition is employed widely in laser cooling experiments [18–21], whereas the  $D1$  transition is used to probe nonlinear optical processes like electromagnetically induced transparency [22] and chip-scale magnetometers [23]. A growing field of study is the modification of the absorptive and dispersive characteristics of a material to control the propagation of light through it [24–26]. There are several uses for absolute absorption spectroscopy in physics, chemistry, metallurgy, and industry [27,28]. It can provide the number density of the ma-

terial being analysed and on being used to measure various spectral lines, it reveals the populations of occupied levels, from which a temperature can be calculated. [29]. Moreover, a signal utilised for frequency reference (locking) of a laser is usually created using *Rb* and *Cs* spectroscopy. Therefore, it becomes necessary to understand the properties of *Rb* and *Cs*. Siddons *et al* considered the thermally moving rubidium atoms in a vapor cell and investigated the Doppler-broadened absorption of a weak monochromatic probe laser beam on *D* lines [19–21] of Rubidium. It is feasible to create sub-Doppler saturation absorption and hyperfine-pumping spectra by counterpropagating a pump beam with the weak probe [30]. They quantitatively predicted the absorptive as well as dispersive behavior of rubidium vapor determined close to the *D* lines. Their results were in agreement with an experimental investigation of the absolute Doppler-broadened absorption spectrum.

A model for computing saturated absorption spectra for dipole transitions in multilevel atoms was developed by Maguire *et al*. They constructed a set of coupled differential equations representing the internal state of atoms in a standing light field by applying semiclassical density matrix approach. They obtained saturated absorption and fluorescence spectra of  $^{85}\text{Rb}$ . This technique predicts significant aspects of saturated absorption spectra quantitatively and with reasonable computing efficiency, such as saturation, crossover resonances, merging of absorption lines at high intensities, and optical pumping between hyperfine levels [31].

## 1.2 Historical Overview of Polarization Spectroscopy

The magnitude of signals obtained in saturation absorption spectroscopy depends on the relative polarization of saturating pump and probe laser beam. The light induced birefringence and dichroism of absorbing gaseous medium are often seen in optical-pumping experiments with incoherent light sources [32]. Yet, it appears that the feasibility and benefit of utilising the resulting optical anisotropy in a sensitive polarisation detection system has remained undiscovered. Wieman and Hansch [2] revealed a novel technique of Doppler-free polarization laser spectroscopy based on light induced birefringence and dichroism of an absorbing gas via a change in light polarization. In this method, a linearly polarized probe beam produced from a monochromatic tunable laser is passed through a gas sample as shown in Figure 1.2. After traveling through a polarizer that is almost completely crossed, just a small portion of this beam reaches a photodetector. Any op-

tical anisotropy that modifies the polarization of the probe wave will change light flux through the polarizer resulting in its detection with high intensity. Sending a pump wave which is circularly polarised through the sample in the reverse direction can produce such an anisotropy. Polarization spectroscopy technique offers a significantly higher signal-to-background ratio comparative to saturated absorption spectroscopy.

In polarization spectroscopy, the linearly polarized probe beam can be considered as superposition of oppositely circularly polarized beams. The pump beam will produce different saturation (*i.e. changes in absorption coefficient and in refractive index*) for these two circular components of probe beam. The probe light will become elliptically polarized due to circular dichroism caused by difference in absorption coefficient whereas a difference in refractive index causes a gyrotropic birefringence which will rotate the axis of polarization. Hence, over a constant background, this birefringent polarisation rotation generates a signal with a dispersion-shape [2, 33].

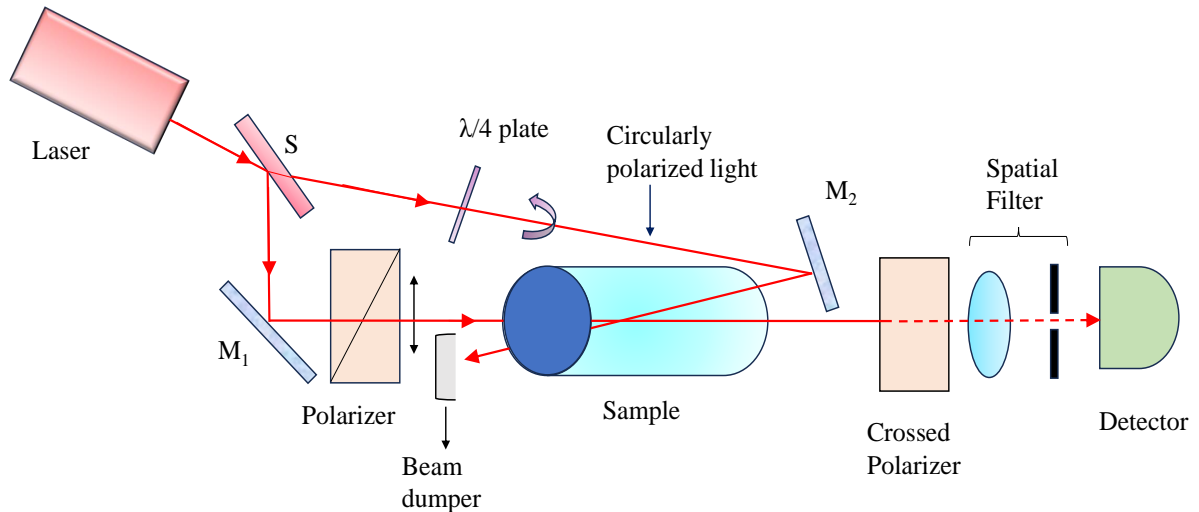


**Figure 1.2:** Experimental scheme of laser polarization spectrometer [2]

Nakayama gave a theoretical model for understanding the polarization spectroscopy

spectra. He integrated the concept of birefringence and dichroism with velocity selective optical pumping [34, 35]. Even while this model yields findings that are very plausible, it is unable to produce a precise theoretical computation of the polarization spectroscopy spectrum. Harris *et al* provided a theoretical description by evaluating rate equations. The transitions from the top hyperfine level of the ground state exhibited agreement with theoretical expectations as per experimental data. Unfortunately, the results for the transitions from the lower hyperfine level of the ground state could not be satisfactorily explained by this model [36].

A theoretical and experimental investigation of the polarisation spectroscopy of rubidium atoms was reported by Huy Diep Do *et al*. They considered all transitions in hyperfine spectra of rubidium atoms. The rate equations were used to determine all of the populations of the magnetic sublevels, which were then utilised to produce the polarization spectroscopy spectra. They performed the calculations for the whole spectrum range, enabling them to get findings that were well in accord with the experimentally observed spectral characteristics, such as the resonance and crossover lines. With high accuracy, they were able to account for each polarization spectroscopy spectrum that was produced for the two rubidium isotopes. The theoretical model created in this study is also applicable to atoms such *Na* or *Cs* [37].

The most important applications of polarization spectroscopy are laser frequency locking [38–43] and spectroscopic measurements in flames [29] and in plasmas [44]. The stimulated Raman scattering and two-photon absorption in gases motivated by related experiments [45, 46] were also facilitated by high-resolution polarization spectroscopy.

## 1.3 Brief History of Imaging Experiments

### 1.3.1 Imaging of a Transparent Object

Although it is widely known from microscopist’s perspective that transparent objects exhibit light or dark contours under the microscope in a variety of ways depending on the change in focus and the type of illumination utilised. Yet the phase object can not be imaged by using a traditional single-lens imaging setup and a conventional intensity-sensitive detector. A phase object is typically imaged in conventional coherent optics either through interferometry or via an optical spatial Fourier-transform system [47],

which transforms the phase distribution in the optical wave front at the object plane into an intensity-sensitive detector-detectable amplitude distribution. F. Zernike found that wave theory has the capability to explaining every detail of the microscopic feature of transparent objects. He invented the phase contrast method for the microscopic observation of transparent objects [48]. The phase contrast method provides a far better indication of the exact details of the object having periodic structure. In addition to this, he also did independent treatment of the phase contrast method for arbitrary objects of irregular structure [49]. A thorough knowledge of imaging the transparent object has been offered by F. Zernike. When a light strikes a microscopic object with slightly absorbing details on a transparent background, absorbing details weaken the light and it gets smaller amplitude. The direct and diffracted vibrations therefore travel to the image point in the same relative phases as they did in the object. Therefore, the background seems lighter while the absorbing details are darker. A transparent object, on the other hand, will cause emerging vibrations to be equal in amplitude but shift in phase relative to incident radiation. As a result, the image will have the same phase differences, which are nonetheless invisible and have a uniform intensity throughout. In ideal case, the phase object is completely invisible [50].

Another scheme to image weakly absorbing materials based on phase contrast method was demonstrated. In this scheme, phase contrast radiography, which instead of recording intensity variations, variations of the phase of the emerging radiation was recorded. This experiment was performed with an X-ray source having high spatial coherence [51]. By resolving phase differences throughout the X-ray beam, Davis *et al.* described a technique for improving contrast in hard X-ray pictures of weakly absorbing materials. Similar to the case of visible light passing through an optically transparent media, the propagation of X-rays via an X-ray transparent medium is accompanied by a change in the wavefront's phase with respect to vacuum [52].

Abouraddy *et al* used beams of entangled photons created via spontaneous parametric down conversion to image a pure phase object. For a phase object, they configured micro electromechanical system micromirror array to modulate the phase of the incident wave front. One of the beams probes the object while the second beam does not interact with the object. The coincidence rate of the photons detected by the two detector is measured as detector (corresponding to second beam) is scanned. They showed theoretically and experimentally that coherent image of the phase object may be obtained by this optical

setup [53]. A transparent phase object also is imaged with quantum entangled photons using ghost diffraction [54] and computational ghost imaging techniques [55, 56]. Classical ghost imaging has also been of considerable interest with thermal light [57].

In another setup, a long path experiment has been performed to quantum image a transparent polarization sensitive phase pattern with hyper-entangled photon pairs involving momentum and polarization degrees of freedom. This transparent phase pattern alters the phase of transmitted photons without absorbing them. This change in phase is position dependent and is different for different polarization of the incident light. One photon interacts with the pattern in the imaging setup, while the second photon, which has never interacted with the pattern, is simultaneously measured in a specified polarization basis as well as in a quantum superposition basis of its position, which is comparable to measuring its momentum. [58].

Another experiment used hyper entangled photons with polarisation and Einstein-Podolsky-Rosen (EPR) entanglement to image a transparent polarization-sensitive phase pattern. By detecting correlations between the polarization-position and polarization-momentum of interacting and non-interacting photons, a quantum ghost image was created. The EPR entanglement links the position states of an interacting photon in the object plane with position states of a non-interacting photon in the image plane, and polarization entanglement enables the detection of the pattern's polarization-sensitive phase shift. [59].

### 1.3.2 Imaging of Bose Einstein Condensate

Absorption imaging of Bose-Einstein condensate is used to measure its temperature and number of atoms. But this technique destroys the condensate. Several techniques have been used to image the Bose Einstein condensate and some of them are described below.

Andrews *et al* noticed that their attempts to directly examine the Bose condensate using absorption imaging failed due to the high optical density of the atom cloud close to the critical temperature. As a result, direct imaging of the condensate is not possible since probe light is totally absorbed, even in the wings of the spatial distribution. However, they demonstrated in their study that dispersively scattered light is able to clearly image the condensate by using the so-called dark ground imaging approach associated with

phase contrast methods discussed above [60]. The birefringence of atomic medium was used for non destructive imaging of the magnetization of an ultracold spin-1 Bose gas. It described how the density and internal state of the atoms being imaged affect the strength of the phase-contrast imaging signal for polarised probing light. In order to resolve the spatial magnetization profile of an optically trapped ultracold gas, polarization-dependent phase-contrast imaging is used [61].

High efficiency detection of ultracold atoms with low noise is often challenging. For this, resonant excitation can be employed, and either the probe light's absorption or the resulting induced fluorescence can be detected. However, optically thick cloud and spontaneously emitted photons which destroys quantum coherence resulting in loss of atoms from the trap makes this task difficult. These difficulties can both be reduced by detuning the light beam to make the medium optically thin and the rate of scattering low. The detection was then performed by measuring the phase shift induced by the atoms impose on the light. This optical phase shift was investigated by interference with a reference beam extracted from the same laser. The dispersion feature was seen when either of the two frequency components tunes through the  $|m = 2\rangle \rightarrow |m' = 3\rangle$  resonance of rubidium  $D_2$  line [62].

Dispersive techniques are often used to image atomic ensembles non-destructively and with high spatial resolution [63]. These dispersive techniques depend on a phase shift imparted to an imaging light by an atomic sample via either the scalar or vector part of the interaction Hamiltonian. The methods based on the vector part utilize the anisotropic response of distinct magnetic substates- generally known as the Faraday effect. Gajdacz *et al* using this effect implemented Dark Field Faraday Imaging (DFFI) for non-destructive measurements of ultracold atomic clouds [64]. A single polarizer was inserted in a standard absorption imaging set-up, thereby making this imaging simpler than the other dispersive techniques. Atoms were prepared in  $|f = 2, m_f = 2\rangle$  state of  $^{87}\text{Rb}$  and for imaging wavelengths are close to the  $D_2$  transition. The polarization plane of initially linearly polarized light is rotated as a result of Faraday rotation. They concluded that DFFI can precisely measure relevant properties of the atomic clouds.

Davis et al. successfully accomplished the Bose-Einstein condensation of sodium atoms. The trapped atomic cloud was pictured using absorption imaging. In order to probe the atoms, 10 mW/cm<sup>2</sup> laser beam in resonance with  $F = 1 \rightarrow F = 2$  transition was first

used to pump the atoms to the  $F = 2$ . Another probing laser pulse in resonance with the  $F = 2 \rightarrow F = 3$  was simultaneously applied to the atoms. A lens system with a resolution of  $8 \mu\text{m}$  was used to image this probe laser onto a charge coupled device sensor. Due to heating, upto 100 photons per atom were absorbed without causing the picture to become blurry. By integrating over the absorption image, the number of atoms were determined [65].

The magnetic field confinement and evaporative cooling were used to create a Bose-Einstein condensate in a vapor of rubidium-87 atoms. To determine the spatial distribution of the trapped atomic cloud, absorption of the circularly polarized laser pulse in resonance with the  $5S_{1/2}$ ,  $F = 2$  to  $5P_{3/2}$ ,  $F = 3$  transition was observed. A charge-coupled device array was used to scan, digitise, and store the cloud's shadow for further examination. The recorded image obtained is the initial velocity distribution projected onto the plane of the image. As a result, both the velocity and coordinate space distributions can be obtained from the single image, which can be used to determine the temperature and central density of the atomic cloud. They suggested that with improvement in measurement sensitivity, atomic cloud can be probed to monitor its dynamics without destruction [66].

### 1.3.3 Imaging in Position Space

Any image localized in a position space is called a position space image. This section describes some of the imaging experiments conducted to image the object located in position space.

Abouraddy *et al* took into consideration a two-photon imaging system in which a high-spatial-resolution detector examines the reference photon's arrival position. This photon is used to investigate a distant (transmissive or scattering) object while another photon arrives at the bucket detector. The photoevent registered by the bucket detector gates the scanned reference detector and an image is captured in the coincidence counts. They gave theoretical arguments about the role of entanglement versus correlation in such a setting. They have illustrated that the image is partially coherent for an entangled two-photon source. However, the imaging is incoherent, if the source produces unentangled but classically correlated photon pairs. They concluded that distributed quantum-imaging setup actually requires entanglement in the source and cannot be realised with a classical

---

source that has correlations but lacks entanglement [67].

Bennink *et al* argued that coincidence imaging can be performed using classical sources and entanglement is not necessary for coincidence imaging. Although classical sources cannot mimic the global statistics of entangled sources, the joint detection statistics which occur in the context of coincidence imaging can be produced using a classical source with the appropriate correlations. They successfully performed the experiment by using classical source made by chopping a laser beam, deflecting it by a variable amount, then passing it through beam splitter [68].

Alejandra Valencia *et al* introduced the concepts of two-photon coherent and two-photon incoherent imaging. Using these concepts, they explained the differences between quantum entangled and classical thermal source. They demonstrated in a experiment the two-photon ghost imaging with thermal radiation. This thermal source allows reproducing in coincidence measurements the ghost image of an object, similarly to the SPDC case, except for a constant background noise [69].

F ferri *et al* showed that the product of the near and far field resolutions obtained using the classical source is better than the entangled case. They performed high-resolution ghost image and ghost diffraction experiments using a single source of classically correlated thermal light. The only advantage of entanglement with respect to classical correlation lies in the better visibility of information [70]. Shapiro *et al* used a pair of bright pseudo-thermal beams possessing a phase-sensitive cross relation as a classical source. They showed that all the features of quantum imaging experiment performed by Barreto Lemos *et al* can be realized in a quantum-mimetic fashion using this source. This source offered a much higher signal-to-noise ratio, thereby greatly reducing image acquisition time compared to that of quantum imaging experiment by Barret Lemos *et al* [71].

So far imaging in position space has been discussed. However, in this dissertation, a novel concept and experiment of phase-space localized patterns and their tomographic imaging introduced by Mandip Singh in Ref [1] will be explained. Such patterns are six-dimensional generalizations of three-dimensional position localized objects. This is different from the conventional imaging experiments where optically responsive objects in position space are imaged using a lens and hence viewed by the human eye. In experiment of Ref [1], objects imaged were three  $2D$  transparent masks. Each mask consisted of an

image of an alphabet of the English script: "C", "A", and "T" respectively. All alphabets were transparent, and the remaining part of each mask was entirely opaque to light. The object laser beam interacted with these objects and imprinted their tomographic images onto the phase space of an atomic medium. These patterns in phase space were localized in unique  $3D$  subspace of  $6D$  phase space spanned by  $\hat{x}$ ,  $\hat{y}$  and  $\hat{p}_z$  coordinates. These tomographic images in phase space were then captured by image laser beam. By varying the frequency of image laser beam, tomographic images at different locations on momentum axis were captured. By combining all the tomographic images, the word CAT is formed. However, method employed in this experiment can imprint and image only light absorbing objects. Suppose, there are alphabets which donot absorb light but exhibit polarization dependent phase shift of the transmitted light. Therefore, these alphabets can modify the polarization of the transmitted light without absorption. The imprinting and tomographic imaging of such polarization-sensitive transparent pattern is the motivation behind the concept and experiment presented in this thesis. The present experiment is different from the Ref [1] experiment for the light absorbing pattern.

## 1.4 Thesis Outline

The chapter 1 : Introduction of the dissertation provides an outline of the complete dissertation. This chapter serves as a brief introduction to each chapter that follows. It provides a quick review of saturated absorption spectroscopy and polarization spectroscopy. The complete description is provided in the individual chapters. Also, this chapter illuminates a succinct history of earlier experiments that were conducted in the relevant field. The final chapter of this dissertation presents an overall overview and conclusion.

In chapter 2 : Atomic Structure of Rubidium , fine and hyperfine splitting in energy levels of  $^{85}Rb$  and  $^{87}Rb$  [72] is discussed. Two different spectroscopic techniques named saturated absorption spectroscopy [5] and polarization Doppler-free spectroscopy technique [2] [5] are employed to resolve the hyperfine energy levels. In saturated absorption spectroscopy [17, 31, 73], two counterpropagating pump and probe beams of the same polarization are allowed to pass through the atomic vapor, and a change in absorption of the probe beam generates signals. However, in polarization Doppler-free spectroscopy [36, 37, 40, 74], the pump is circularly polarized, and the probe is linearly polarized. A polarization-dependent change in the refractive index of the medium due to

the pump beam produces a change in the plane of polarization of probe light, which is detected to produce a locking signal. In both experiments, a single-mode extended cavity diode laser is used. The linewidth of the laser is  $< 1$  MHz at 780 nm and mode hop free spectral range is 7 – 8 GHz.

This chapter 3 : *3D* Tomographic Imaging in Phase Space introduces an entirely new concept of phase space imaging [1]. It is known that in conventional imaging experiments, optically responsive objects in position space can be imaged using a lens and hence viewed by the human eye. The work described in this chapter goes beyond this usual imaging in position space and explains the concept of imaging phase space patterns. The pattern in phase space cannot be imaged with a lens conventionally and cannot be seen by the human eye. It is explained in this chapter, how a stationary structural pattern is created and imprinted onto the phase space of an atomic gaseous medium at room temperature, and tomographically imaged. The experiment is based on the concept of velocity selective hole burning [3,75] in the Doppler broadened absorption profile [76] of an atomic gaseous medium [4].

In this experiment, an atomic gaseous medium considered is a 10 cm long rubidium ( $^{87}\text{Rb}$ ) vapor cell insulated from an external magnetic field. Objects to be imaged are three *2D* transparent masks. Each mask consists of an image of an alphabet of the English script: C (on mask-1), A (on mask-2), and T (on mask-3). All alphabets are transparent, and the remaining part of each mask is entirely opaque to light. The three object laser beams carrying the intensity profiles of these masks are allowed to pass through the atomic medium. A counterpropagating linearly polarized imaging laser beam is overlapped with the object laser beams traveling through the atomic gaseous medium to picture this localized pattern. If the imaging laser beam interacts with a velocity class of atoms excited by object laser beams, its absorption reduces. This produces velocity-selective hole burning in the Doppler broadened absorption profile of the atomic medium.

The frequency spread of all laser beams is less than 1 MHz. The object laser beam is extracted and red detuned by 190 MHz from the resonant transition. On a non polarization beamsplitter, this extracted object laser light is overlapped with the imaging laser of the same polarization. A quick response photodetector detects the beating signal of two lasers, which is then analyzed using a radiofrequency spectrum analyzer. The frequency of the beating signal, which corresponds to a frequency difference between two lasers, is

used to determine the detuning. The frequency detuning of beams is measured with a resolution 0.1 MHz.

In chapter 4 : Sub tomographic imaging of a birefringent phase pattern localized in a phase space , which is an experiment to imprint a transparent birefringent phase pattern onto the phase space of an atomic gaseous medium is described. The experiment is conducted with gaseous  $^{87}\text{Rb}$  atoms confined in a glass cell. The concept of atomic-state dependent velocity selective hole burning [3, 75] serves as the foundation of this experiment. Two separate single-mode extended cavity diode lasers, each with a linewidth of 1 MHz, are used to produce imprinting and imaging laser beams. Both beams are frequency locked to the  $D_2$  transition of the  $^{87}\text{Rb}$  at  $\lambda = 780\text{ nm}$  and the frequency of imaging laser light can be shifted by acousto-optic modulators.

The measurement of the precise frequency difference between two laser beams is crucial for carrying out this experiment. This is done by extracting the imprinting laser light and shifting its frequency by  $-110\text{ MHz}$ . This frequency-shifted beam is overlapped with another extracted imaging laser light on a fast response photodetector. These two laser beams interfere in the time domain with a beat frequency equal to a difference in laser frequencies. A radio frequency analyzer measures the frequency of a laser beat signal and assesses the detuning of the imaging laser beam.

The position localized  $2D$  transparent birefringent phase pattern is created with a spatial light modulator (SLM). Direct imaging of this pattern with a camera does not yield an intensity image. To image this pattern, both the imaging and imprinting laser beams are allowed to propagate through the glass cell. After traveling through the atomic medium, the rotation of a plane of polarization of the imaging laser beam is analyzed by a polarizer. An EMCCD camera measures its transverse intensity profile to construct a sub-tomographic image. Four different images are acquired for 200 ms time of exposure on the camera. Each image is separated by a time interval of 700 ms. This chapter explains how two sub-tomographic images are obtained in the experiment. Furthermore, the pattern is localized in a unique  $3D$  subspace of a  $6D$  phase space formed by two position coordinates  $(x, y)$  and one momentum coordinate  $p_z$ .

The conclusions of the foundational experiments conducted in the lab are summarized in the chapter 5 : Conclusion. This chapter concludes the saturation absorption spectroscopy and polarization spectroscopy experiments. Furthermore, it encompasses the summary

---

of an experiment conducted to image transparent birefringent phase object localized in phase space.



# Chapter 2

## Atomic Structure of Rubidium

### 2.1 Introduction

The coupling of the electron's spin magnetic moment with the magnetic field of the proton gives rise to fine structure effects. This coupling causes splitting in the energy levels of the electronic state. These fine energy levels are further split into hyperfine energy levels. This hyperfine splitting in energy levels of the electronic state is due to the interaction of the electromagnetic field produced by the electrons at the nucleus with the electromagnetic multipole moments possessed by the nucleus. In this chapter, we will discuss the fine and hyperfine splitting in energy levels of  $^{85}\text{Rb}$  and  $^{87}\text{Rb}$ . These hyperfine energy levels are not resolved due to Doppler broadening. This chapter mainly focuses on overcoming this limitation. We are going to discuss two different spectroscopic techniques viz saturated absorption spectroscopy [5] and polarization doppler free spectroscopy technique [2] [5]. In saturated absorption spectroscopy, two counterpropagating pump and probe beams are allowed to pass through the atomic vapor. The absorption of the pump beam increases when it matches the resonant transition frequency of an atom, thereby increasing the transmission of the probe beam. This change in absorption of the probe beam generates signals in saturated absorption spectroscopy. However, in polarization Doppler-free spectroscopy, the pump wave causes a change in the absorption coefficient  $\alpha$  and a change in refractive index  $n$ . The signals in the latter arise due to the change in the probe light polarization state induced by a polarized pump wave.

## 2.2 Fine structure

The fine structure arises due to the coupling of the electron's spin magnetic moment with the proton's magnetic field. It is known that an electron with charge  $-e$  and orbital angular momentum  $\vec{L}$  rotates around the positively charged ( $Ze$ ) nucleus. This circular motion produces a magnetic moment given by [77]:

$$\vec{\mu}_s = -\frac{e}{m_e c} \vec{S} \quad (2.1)$$

The  $\vec{S}$  has a magnitude of  $\sqrt{S(S+1)}\hbar$ , here  $S$  is the spin quantum number. Now let us transform to a reference frame in which electron is at rest at origin. From this frame of reference, a nucleus can be seen moving with the frequency  $\nu_n$  around the electron at radius  $r$ . The motion of the nucleus is equivalent to a current carrying loop, and the current is equal to  $Ze\nu_n$ . This current will produce a magnetic field at the location of the electron [77]:

$$\vec{B}_l = \frac{1}{em_e c r} \frac{dV}{dr} \vec{L} \quad (2.2)$$

For Hydrogen like atoms, a single valence electron moves in the central potential of the nucleus represented by  $V(r)$ . Due to two spin orientations  $S_z = \pm\hbar/2$ , the magnetic spin moment of the electron can be aligned spatially in two directions in this field. The torque due to the magnetic field in Equation 2.2 will try to align the magnetic moment of the electron along the direction of the field. The Hamiltonian of the combined system is [77]:

$$\hat{H}_{SO} = -\vec{\mu}_s \cdot \vec{B} = \frac{1}{m_e^2 c^2 r} \frac{dV}{dr} \vec{S} \cdot \vec{L} \quad (2.3)$$

It is important to note that the rest frame of the nucleus is not the inertial one. This can be corrected by Thomas precession where factor  $1/2$  is incorporated in the expression:

$$\hat{H}_{SO} = \frac{1}{2m_e^2 c^2 r} \frac{dV}{dr} \vec{S} \cdot \vec{L} \quad (2.4)$$

It is better to use eigen states of  $L^2$ ,  $S^2$ ,  $J^2$ , and  $J_z$  as Hamiltonian no longer commutes with  $\vec{L}$  and  $\vec{S}$ . This implies that the spin and orbital angular momentum are not conserved separately. Introducing the total angular momentum [78]

$$\vec{J} = \vec{L} + \vec{S} \quad (2.5)$$

where  $\vec{J}^2 = J(J+1)\hbar^2$  and  $\vec{L}^2 = L(L+1)\hbar^2$ . So the scalar product  $\vec{L} \cdot \vec{S}$  is given by:

$$\vec{L} \cdot \vec{S} = \frac{1}{2}\hbar^2[J(J+1) - L(L+1) - S(S+1)] \quad (2.6)$$

The energy correction due to the spin orbit coupling is [77]:

$$E_{SO} = \frac{e^2\hbar^2}{2m_e^2c^2} \frac{J(J+1) - L(L+1) - 3/4}{n^3l(2L+1)(L+1)a_0^3} \quad (2.7)$$

It should be emphasized here that there is no fine structure splitting for  $s$ -states ( $L = 0$ ). The splitting in energy levels due to fine structure occurs only for  $L \geq 1$  levels.

## 2.3 Hyperfine structure

The observation of fine structure with very high spectral resolution reveals that it is further split into subcomponents. These subcomponents are referred to as hyperfine structure. When the electromagnetic field produced by the electrons at the nucleus interacts with the electromagnetic multipole moments possessed by the nucleus, energy levels of electrons are altered, resulting in hyperfine splitting. Depending upon the nuclear spin, hyperfine splitting is different for different multipole moments of the nucleus. However, the multipole moments possessed by the nucleus are quite restricted. The odd-order magnetic moments and even-order electric moments are the only non-vanishing nuclear multipole moments. The discussion below focuses on the hyperfine structure due to magnetic dipole and electric quadrupole hyperfine interaction [79].

### 2.3.1 Magnetic Dipole Interaction

In atom, nucleus is confined in a small but finite volumed region. In addition to an electric charge of  $Ze$ , it also possess a nuclear spin. In analogy to the electron spin, nuclear spin has absolute value given by [80]:

$$|\vec{I}| = \sqrt{I(I+1)}\hbar$$

The operator  $\vec{I}_z$  has eigen values  $m_I\hbar$  with  $-I \leq m_I \leq +I$ . Consider the nucleus to be point dipole having magnetic dipole moment given by:

$$\vec{\mu}_N = \gamma_k \vec{I} \quad (2.8)$$

In terms of nuclear magneton, the same expression can be written as:

$$\vec{\mu}_N = g_n \frac{\mu_k}{\hbar} \vec{I} \quad (2.9)$$

where  $\mu_k = \frac{e\hbar}{2M_p} = \frac{m_e}{M_p} \mu_B$  is the nuclear magneton,  $M_p$  is the mass of the proton and  $\mu_B$  is the Bohr magneton.

The interaction of the nuclear dipole moment  $\vec{\mu}_N$  with the magnetic field  $-(\mu_0/4\pi)e\vec{L}/mr^3$  created at the nucleus by the rotation of the electronic charge is represented by the following Hamiltonian [79]:

$$H_1 = \frac{\mu_0}{4\pi} \frac{2}{\hbar^2} g_n \mu_B \mu_k \frac{1}{r^3} \vec{L} \cdot \vec{I} \quad (2.10)$$

It is important to note that there is no energy correction for this term for  $L = 0$  as  $H_1$  has non-zero matrix elements only between states for which  $L \neq 0$ . Now, the other interaction which alters the electronic energy levels is due to the interaction of electronic magnetic moment  $\vec{\mu}_S$  with the nuclear magnetic moment  $\vec{\mu}_N$ . It is given by the following Hamiltonian [79]:

$$H_2 = -\frac{\mu_0}{4\pi} \frac{2}{\hbar^2} g_n \mu_B \mu_k \left[ \vec{S} \cdot \vec{I} \nabla^2 \left( \frac{1}{r} \right) - (\vec{S} \cdot \vec{\nabla})(\vec{I} \cdot \vec{\nabla}) \frac{1}{r} \right] \quad (2.11)$$

It is more easier to look at the term  $H_2$  for the two instances  $r \neq 0$  and  $r = 0$  separately. This expression at  $r = 0$  is only relevant for states with  $L = 0$  states. For  $L = 0$ ,  $H_1$  will not contribute, so the only correction will come from this term.

$$H_2(\text{at } r = 0) = -\frac{\mu_0}{4\pi} \frac{8\pi}{3} \vec{\mu}_s \cdot \vec{\mu}_N \delta(\vec{r}) \quad (2.12)$$

For  $r \neq 0$ , both term  $H_1$  and  $H_2$  will contribute, so their combined hamiltonian is given by [79]:

$$H_{Total} = \frac{\mu_0}{4\pi} \frac{2}{\hbar^2} g_n \mu_B \mu_k \frac{1}{r^3} \left[ \vec{L} \cdot \vec{I} - \vec{S} \cdot \vec{I} + 3 \frac{(\vec{S} \cdot \vec{r})(\vec{I} \cdot \vec{r})}{r^2} \right] \quad (2.13)$$

The diagonalization of the perturbation is substantially facilitated by the introduction of the total angular momentum of the atom, analogous to the spin orbit coupling:

$$\vec{F} = \vec{I} + \vec{J} \quad (2.14)$$

We will represent the eigenvalues of the operator  $F^2$  by  $F(F+1)\hbar^2$  and those of  $F_z$  by  $M_F \hbar$  with  $M_F = -F, -F+1, \dots, F$ . The energy shift due to Hamiltonian in Equation 2.13

is [79]:

$$\Delta E = \frac{C}{2}[F(F+1) - I(I+1) - J(J+1)] \quad (2.15)$$

with

$$C = \frac{\mu_0}{4\pi} 4g_n \mu_B \mu_k \frac{1}{J(J+1)(2L+1)} \frac{Z^3}{a_\mu^3 n^3} \quad (2.16)$$

where  $J = S$  for  $s$ -states. The combination of the aforementioned results with the selection rules for electromagnetic transitions between energy levels will provide the hyperfine structure of spectral lines resulting from the magnetic dipole interaction. The selection rules  $\Delta L = \pm 1$  and  $\Delta J = 0, \pm 1$  remain valid for electric dipole transitions, and in addition to this the quantum number  $F$  follows selection rule given by:

$$\Delta F = 0, \pm 1 (\text{excluding } F = 0 \rightarrow F = 0) \quad (2.17)$$

### 2.3.2 Electric Quadrupole Hyperfine Interaction

Another important characteristic of the structure of a nucleus is the electric quadrupole moment. The energy corresponding to the interaction of electric quadrupole moment of the nucleus with the electrostatic potential  $V_e$  created by an electron at the nucleus is given by [79]:

$$H_{EQ} = B \frac{\frac{3}{2} \vec{I} \cdot \vec{J} (2\vec{I} \cdot \vec{J} + 1) - \vec{I}^2 \vec{J}^2}{2I(2I+1)J(2J+1)} \quad (2.18)$$

where the quadrupole coupling constant  $B$  is given by

$$B = Q \left\langle \frac{\delta^2 V_e}{\delta z^2} \right\rangle \quad (2.19)$$

The first order energy shift due to the electric quadrupole interaction is:

$$\Delta E = \frac{B}{4} \frac{\frac{3}{2} K(K+1) - 2I(I+1)J(J+1)}{I(2I-1)J(2J+1)} \quad (2.20)$$

where  $K = F(F+1) - I(I+1) - J(J+1)$ . There is no quadrupole energy shift for  $s$ -states because  $\langle \frac{\delta^2 V_e}{\delta z^2} \rangle$  vanishes for spherically symmetric charge distribution of electronic charge. Also, there is no electric quadrupole moment for nuclei with no spin ( $I = 0$ ) or a spin  $I = 1/2$ , so energy shift vanishes in this case too. The total hyperfine structure energy correction is obtained by addition of electric quadrupole correction to the magnetic dipole

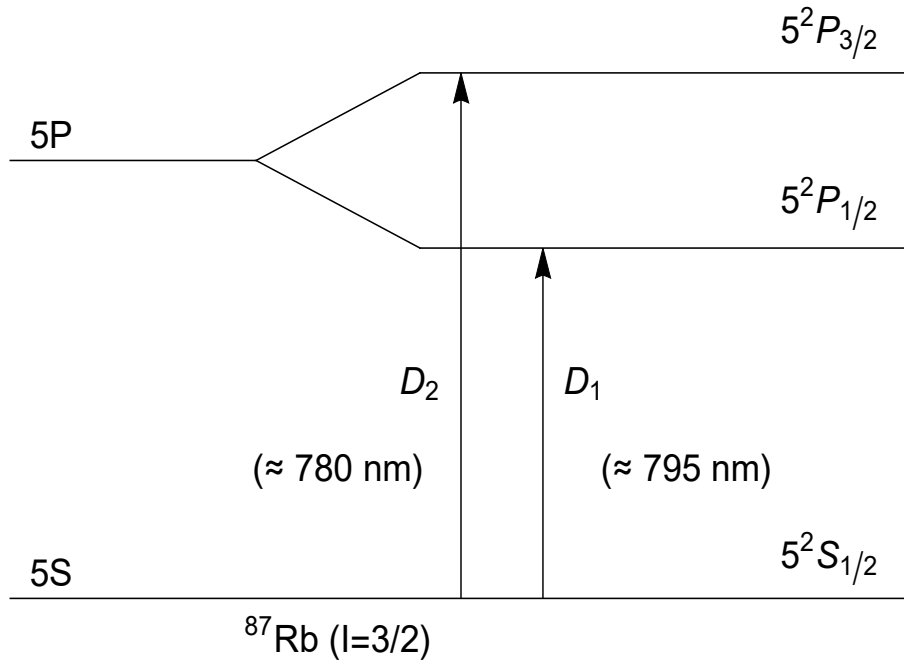


**Figure 2.1:** Fine structure of  $^{87}\text{Rb}$  due to spin-orbit coupling

shift and is given by:

$$\Delta E = \frac{C}{2}K + \frac{B}{4} \frac{\frac{3}{2}K(K+1) - 2I(I+1)J(J+1)}{I(2I-1)J(2J+1)} \quad (2.21)$$

## 2.4 Rubidium Atoms

Rubidium is an ideal atomic medium from an experimental standpoint since it has a sufficient vapor pressure at room temperature to provide significant absorption in vapor cell. Additionally, the  $D$  lines for these atoms appear at wavelengths where reliable and affordable laser diode sources are available [76]. The electronic configuration of the Rubidium is  $[Kr]5s^1$ . Its energy levels have a reasonably straightforward hydrogen like structure since it only has one electron outside of closed shells. Rubidium has two isotopes,  $^{85}\text{Rb}$  and  $^{87}\text{Rb}$ , with a natural abundance of 3 : 1. The rubidium sample cell used in this experiment contains  $^{85}\text{Rb}$  and  $^{87}\text{Rb}$  in natural abundances of 72.17% and 27.83%

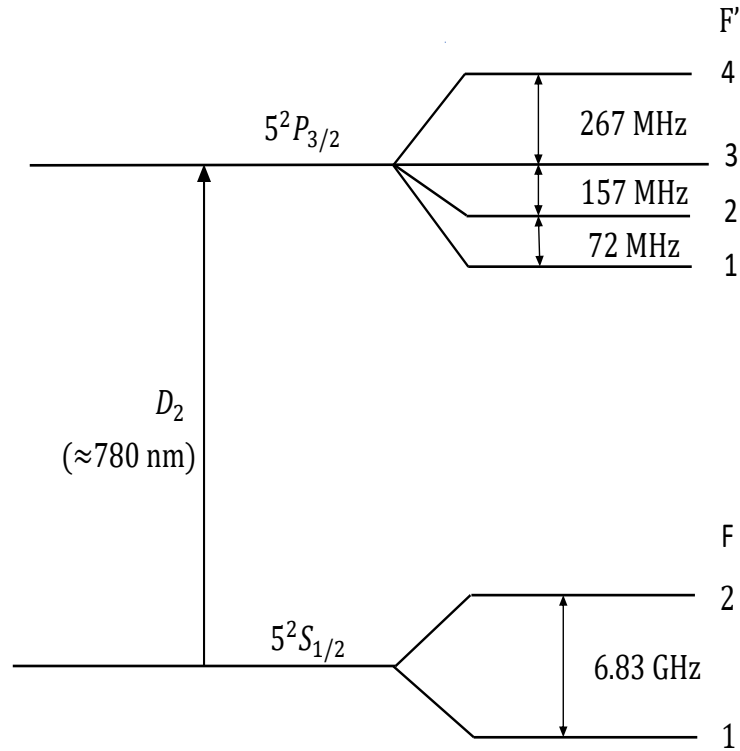


**Figure 2.2:** Hyperfine splitting of energy levels in  $^{87}\text{Rb}$

respectively [81]. Here the convention used for the magnitude of  $\vec{J}$  is  $\sqrt{J(J+1)}\hbar$ . The outer most electron's orbital angular momentum  $\vec{L}$  and spin angular momentum  $\vec{S}$  couple together to yield fine structure  $\vec{J} = \vec{L} + \vec{S}$ . As already discussed in section 2.2, we can see in Figure 2.1 that there is no fine structure splitting for  $L = 0$  ground state. The excited state due to fine structure splits into two states with  $J = 1/2$  or  $J = 3/2$ . Therefore, the  $D$  line ( $L = 0 \rightarrow L = 1$ ) transition splits into two components, the  $D_1$  line ( $5^2S_{1/2} \rightarrow 5^2P_{1/2}$ ) and the  $D_2$  line ( $5^2S_{1/2} \rightarrow 5^2P_{3/2}$ ). Now, these fine structure components will further split into hyperfine components [82–84] due to the coupling of  $J$  with the total nuclear angular momentum  $I$ . This coupling will yield the total atomic angular momentum  $F$  given by  $\vec{F} = \vec{J} + \vec{I}$  and the magnitude of  $\vec{F}$  can take the values  $|J - I| \leq F \leq |J + I|$ . Accordingly, hyperfine splitting in ( $^{87}\text{Rb}$ ) rubidium is illustrated in Figure 2.2 : for the ground state ( $5^2S_{1/2}$ ),  $F$  is either 1 or 2, so there are two hyperfine energy level and for excited state

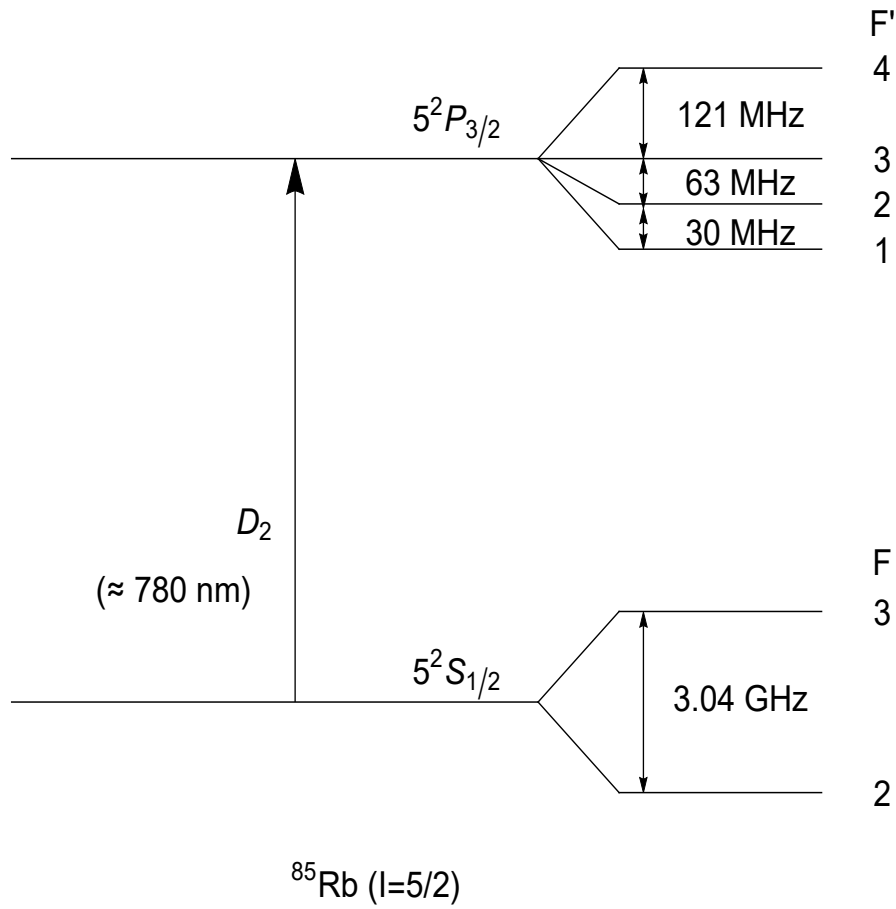


**Figure 2.3:** Hyperfine splitting of energy levels in  $^{85}\text{Rb}$

( $5^2P_{3/2}$ ),  $F$  can take any of the values 1, 2, 3 and 4 [72]. The hyperfine energy levels for the  $^{85}\text{Rb}$  is shown in Figure 2.3. It can be seen in Figure 2.1, for  $D_2$ ,  $\lambda = 780 \text{ nm}$  [85] and  $\Gamma = 2\pi 6.065 \text{ MHz}$  [86]. whereas for  $D_1$ ,  $\lambda = 794.979 \text{ nm}$  [85], [87],  $\Gamma = 2\pi 5.746 \text{ MHz}$  [86]. In the presence of external magnetic field, each level with specific  $F$  value splits into  $2F + 1$  Zeeman sublevels known as Zeeman effect, where splitting in energy levels is given by  $E_{(m_F)} = g_F m_F \mu_B |\vec{B}|$ ;  $g_F$  is the gyromagnetic ratio,  $\mu_B$  is Bohr magneton,  $|\vec{B}|$  is the magnitude of applied magnetic field. [88].

## 2.5 Doppler Broadening

If a laser beam is permitted to pass through an atomic medium, transition between distinct energy levels will take place due to the absorption of light. The light absorption by the

medium depends upon the laser intensity and its frequency in relation to the resonant frequency of atoms ( $\nu_0$ ) in the medium. However, each energy level has a linewidth, so the absorption will take place over a range of frequencies rather than a single precise frequency. The absorption profile after passing through the atomic medium is Lorentzian in shape given by following equation [80]:

$$I(\omega) = I_0 \frac{\Gamma/2\pi}{(\omega - \omega_0)^2 + (\Gamma/2)^2} \quad (2.22)$$

Here,  $\Gamma$  is the natural linewidth of a particular transition. This so called natural linewidth is due to the finite time of the electronic energy state. It does put a limit on the achievable accuracy of the measurement of spectral lines. However, it has been observed in real situations that width of a transition is generally larger than the natural linewidth ( $\Gamma$ ). This broadening occurs due to different broadening mechanism like pressure broadening, collision broadening and Doppler broadening. For this experiment, we focus on Doppler broadening. The Doppler broadening arises due to the random thermal motion of the atoms in the medium. At room temperature, atoms move with an approximate average speed of  $300 \text{ m s}^{-1}$ . Thus, if this medium is irradiated by laser light, thermal motion will cause most of atoms to receive incident light at frequencies shifted away from the laser frequency. If laser's frequency matches atomic resonant frequency, atoms having no velocity component along the direction of incident light will absorb this light. Suppose laser beam is incident along  $z$ -direction, then atoms having velocity component along incident direction will absorb light only when laser frequency is tuned to [76]:

$$\omega = \omega_0 \left( 1 + \frac{v_z}{c} \right) \quad (2.23)$$

where  $c$  is the speed of light and  $\omega_0$  is the resonant frequency of an atom at rest. This is the equation for the case  $v_z \ll c$ . Because of the distribution in atomic velocities, there will also be a distribution of light frequencies that can be absorbed by the atoms in the medium, even for a single atomic transition. At thermal equilibrium, we can assume that the velocities in the atomic medium will follow a classical Maxwellian distribution. The probability of an atom having velocity between  $v_z$  and  $v_z + dv_z$  is given by the Maxwellian distribution:

$$P(v_z)dv_z = \sqrt{\frac{m}{2\pi kT}} \exp\left(-\frac{mv_z^2}{2kT}\right)dv_z \quad (2.24)$$

where  $m$  is the mass of an atom and  $T$  is the absolute temperature. In terms of observed transition frequency ( $\omega$ ), the above expression can be re-written as:

$$P(\omega) \propto \sqrt{\frac{m}{2\pi kT}} e^{-\frac{(\omega-\omega_0)^2}{\omega_0^2 \frac{m c^2}{2kT}}} \quad (2.25)$$

By using Maxwell Boltzmann statistics, we can define the full width half max to be:

$$\Delta\omega = 2\omega_0 \sqrt{\frac{2k_B T}{m c^2} \ln 2} \quad (2.26)$$

This expression represents Doppler width. Saturation absorption spectroscopy can be used to overcome this spectral resolution limitation.

## 2.6 Saturation Absorption Spectroscopy

The subtle details of the atomic or molecular structure can be seen with the use of Doppler free spectroscopy techniques [5]. The hyperfine structure of an atomic gaseous medium is mainly hidden by Doppler broadening. The saturated absorption technique circumvents this limitation due to Doppler broadening without cooling down the sample. The hyperfine transitions are resolved down to their natural linewidth, typically orders of magnitude less than the Doppler width. This technique is used to lock laser frequencies to particular atomic transitions. It plays a crucial role in high-resolution spectroscopy and cooling and trapping of atoms.

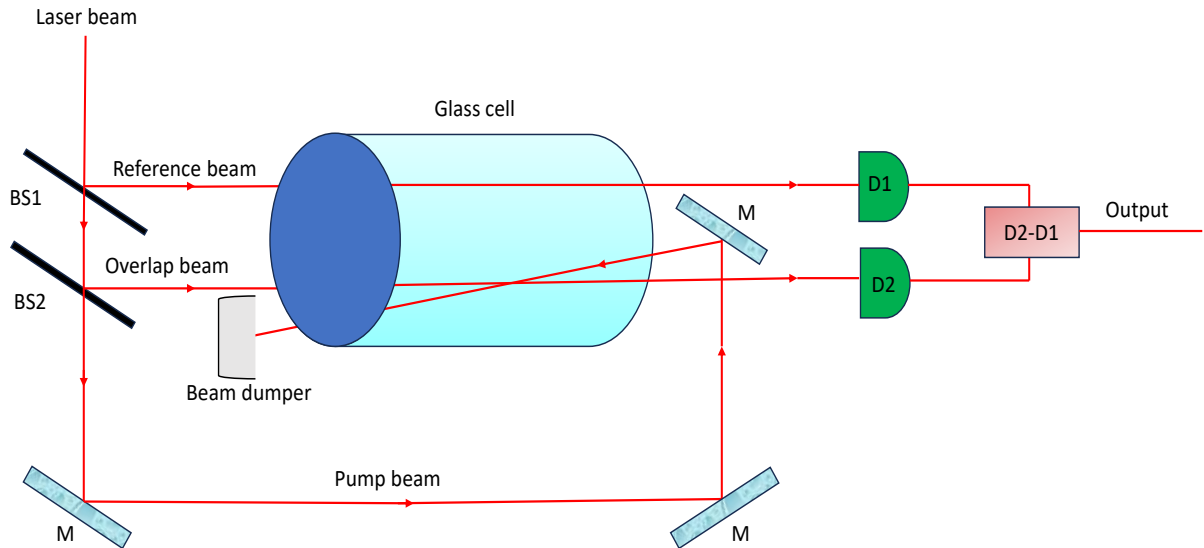


**Figure 2.4:** Experimental setup for Saturated Absorption Spectroscopy: Beam Splitter (BS); Mirror (M); Photodiode ( $D_1$  and  $D_2$ )

### 2.6.1 Theory

The Doppler free spectroscopy is based on the nonlinear interaction of laser light with atoms to achieve Doppler free spectra of atomic gases [5]. This technique commonly called saturated absorption spectroscopy has revolutionized spectroscopic studies. In this technique, light beam from the laser is split into three beams and is allowed to traverse through the atomic vapor. The frequency of the laser is varied, and when this frequency matches transition frequency of the atom, increase in absorption is observed.

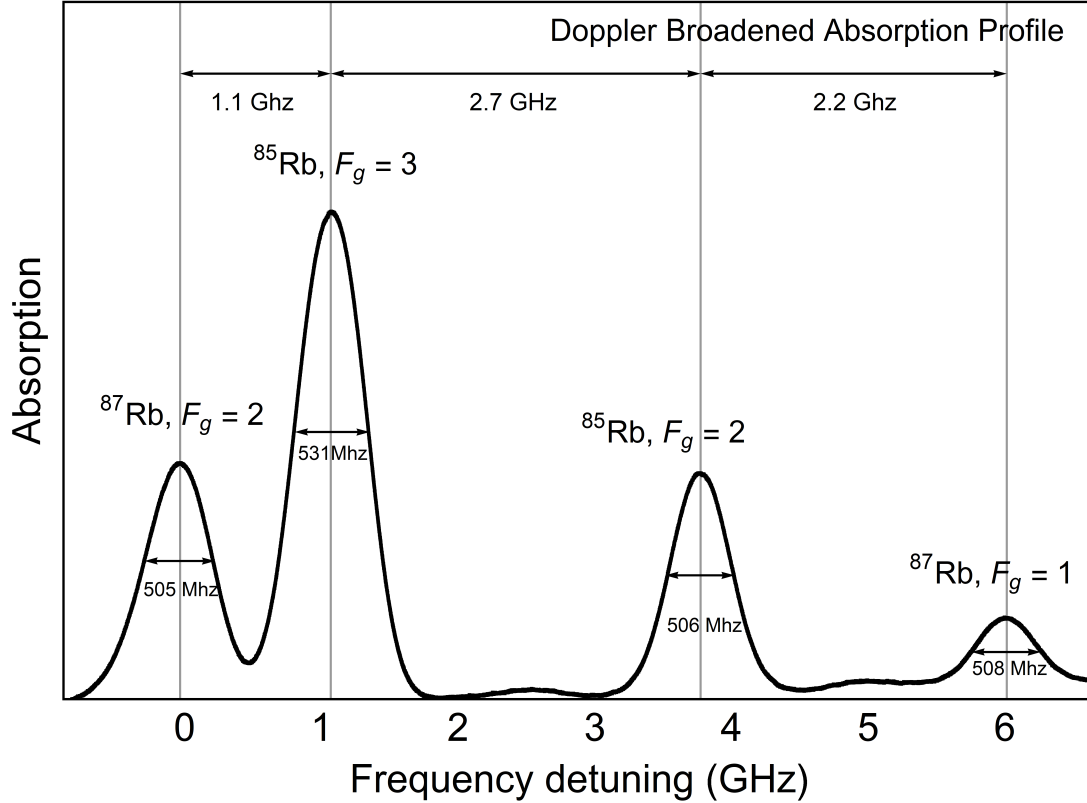


**Figure 2.5:** Doppler broadened spectral lines for  $^{87}\text{Rb}$  and  $^{85}\text{Rb}$

In the experiment, probe beam is propagating along the positive  $z$ -direction. The pump beam is propagating along negative  $z$ -direction. Depending upon the velocity, different subgroups of atoms will absorb the pump and probe beams as explained below [76].

- When the frequency of the laser is greater than the resonant frequency of the atoms in the medium ( $\nu_L > \nu_0$ ), the pump beam will be in resonance with the atoms having  $v_z < 0$ , whereas the probe beam will interact with the different velocity group of atoms for which  $v_z > 0$ . In other case, consider the laser frequency to be less than the resonant frequency ( $\nu_L < \nu_0$ ). The pump beam will then interact with the atoms subgroup having  $v_z > 0$  and probe wave will excite the atoms having  $z$  velocity component i.e.  $v_z < 0$ .

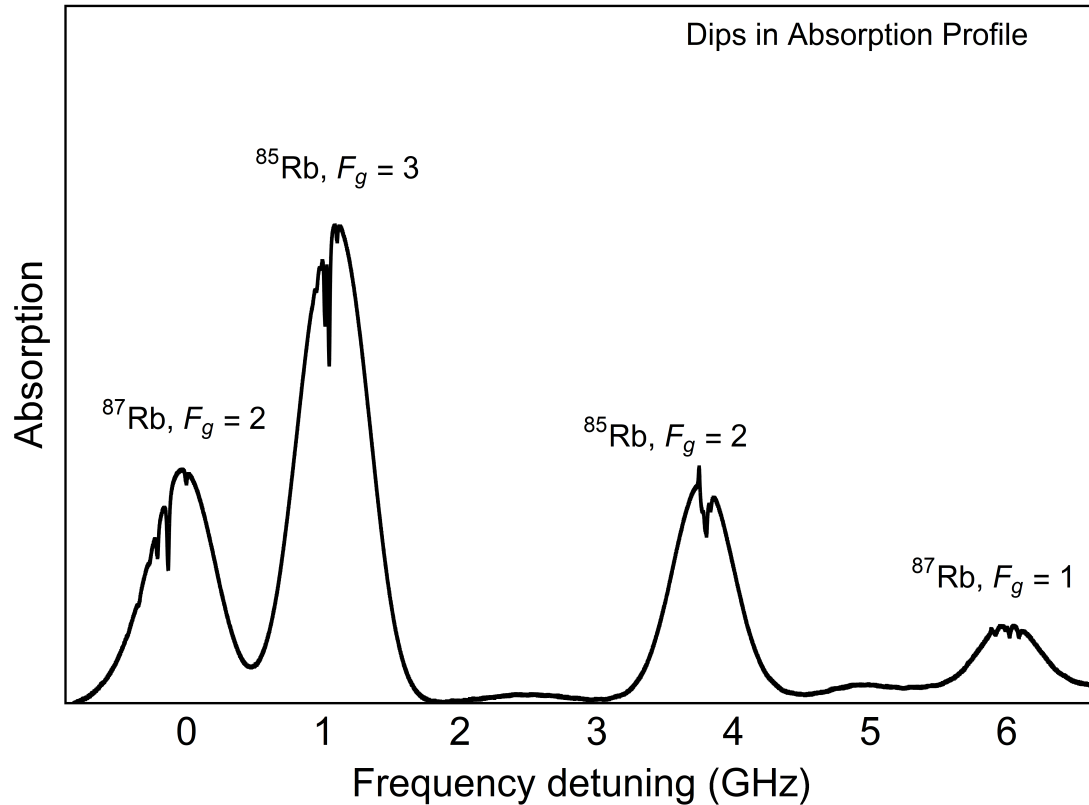


**Figure 2.6:** Doppler broadened lines with dips representing hyperfine structure of  $^{87}\text{Rb}$  and  $^{85}\text{Rb}$ .

- When the laser frequency matches the resonance frequency of the atoms, both the pump and probe beam will interact with the same subgroup of atoms of velocity  $v_z = 0$ . Consequently, the pump beam will saturate this atomic transition and the population of atoms in ground state will deplete. In this circumstance, absorption experienced by the probe wave will be greatly reduced.

### 2.6.2 Experimental Setup

The schematic diagram for saturation absorption spectroscopy is shown in Figure 2.4. In this experiment, a single mode extended cavity diode laser is used. The linewidth of the laser is about  $< 1$  MHz at 780 nm and mode hop free spectral range is 7 – 8 GHz. The light from the laser is divided into three beams. The most intense (of the order of the

saturation intensity of the transition) beam is the pump beam while the other two beams, which are of considerably lower intensity than the pump beam are probe beams.

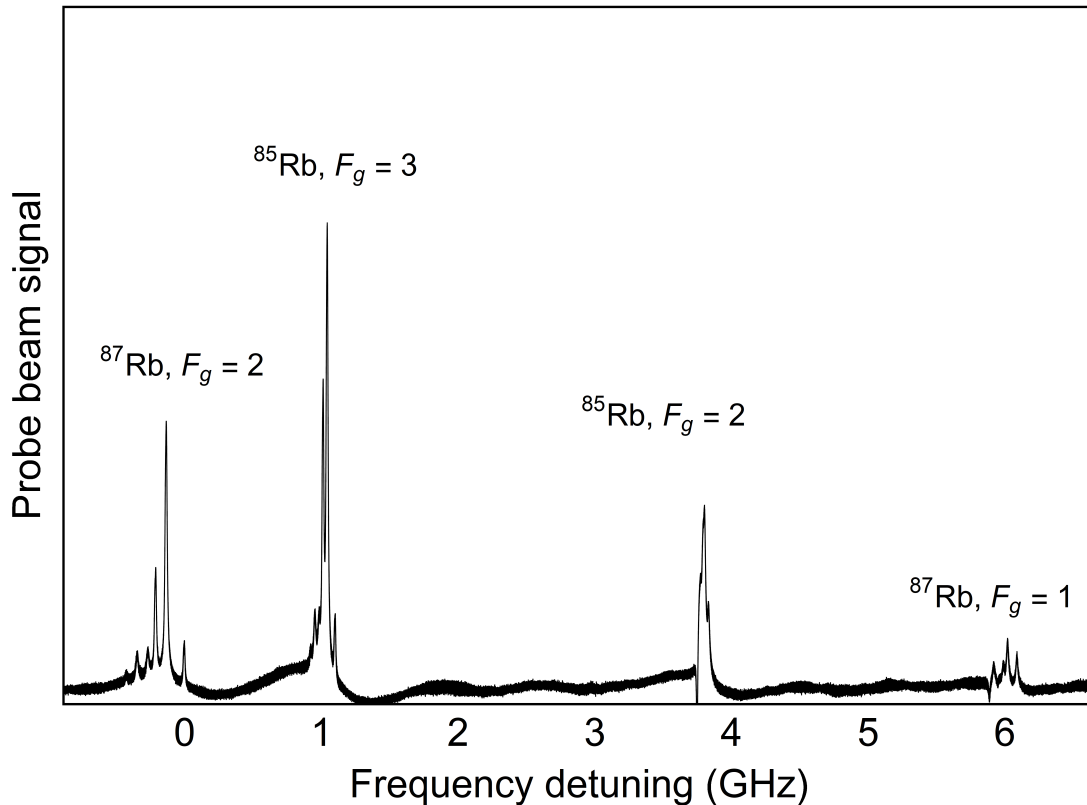


**Figure 2.7:** Saturated absorption lines

The intensity of probe beam is much lower than the saturation intensity of the transition under consideration. These probe beams are sent through the vapor cell in the opposite direction to that of the pump beam. The probe beam that intersects the counter-propagating pump beam inside the cell is called the overlap probe beam, and the other beam that does not cross the pump beam is known as the reference probe beam. A slight crossing angle between the two beams results in a residual doppler width. If the pump and probe beams are strictly anticollinear, the probe beam is coupled back into the laser, resulting in laser instabilities. The signals generated by the two probe beams at the photodiode are adjusted to be equal before subtracting from each other. In the experiment performed in the laboratory, spectrum is obtained by recording the difference

between these two signals as laser frequency is varied. In this technique, firstly overlap probe beam is blocked so it does not reach the photodiode, the absorption signal then comes from the reference probe beam. This signal from reference beam displays Doppler broadened absorption profiles. This well-known effect arises because the atoms have a thermal (Maxwellian) distribution of velocities.

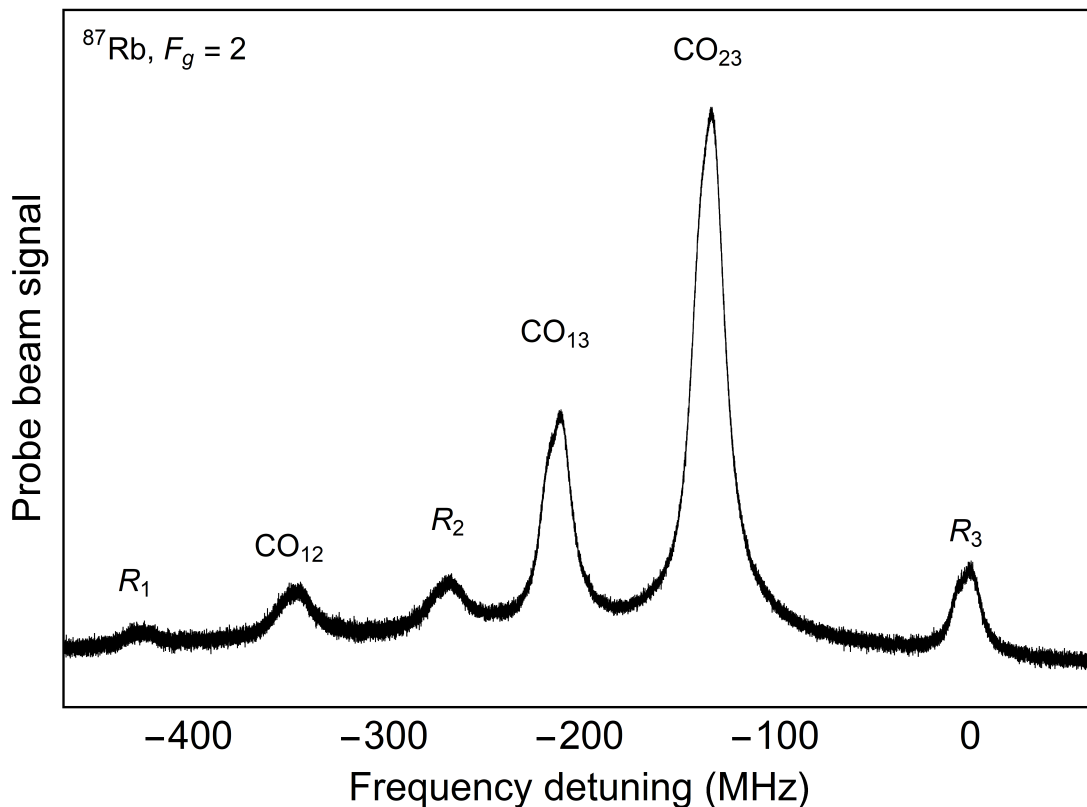


**Figure 2.8:**  $F_g = 2 \rightarrow F_e = 1, 2, 3$  transitions for  $^{87}\text{Rb}$

In the presence of pump beam, when the laser frequency is different from the resonant frequency of Rubidium ( $^{87}\text{Rb}$ ) atoms  $\nu_0$ , one beam (probe beam) interacts with a set of atoms with velocity  $v_z$ , and the other beam (pump beam) interacts with an entirely different set of atoms those with velocity  $-v_z$ . However, when the frequency is tuned to  $\nu_0$  (resonant frequency of atom), the two beams interact with the same group of atoms, those with velocity components perpendicular to the beam. Under these circumstances, the stronger pump beam reduces the absorption experienced by the weaker overlap probe

beam but only over a very narrow range of frequencies that under proper conditions can approach the natural width determined by the lifetime of an atomic transition. This decrease in absorption will appear as a dip in Doppler broadened absorption spectrum. This phenomenon is known as hole-burning. As we tune the laser through a range of frequencies, transitions among the different excited states can be induced resulting in various dips in the spectrum. However, in addition to real transitions, the interaction of laser light with different velocity groups of atoms can also induce crossover peaks [5,30,76]. A crossover resonance occurs when two transitions share a common ground state and differ in frequency by less than the Doppler width. A higher transition has frequency  $\nu_2$  and lower transition has frequency  $\nu_1$  (both from common ground state). The crossover then occurs at some laser frequency  $\nu_c$  such that the same group of atoms will be resonant at  $\nu_1$  with the pump and at  $\nu_2$  with the probe. The crossover frequency  $\nu_c$  is given by [76]:

$$\nu_c = \frac{\nu_1 + \nu_2}{2} \quad (2.27)$$

The spectrum obtained using this experimental setup is shown in Figure 2.5. Plot 2.5 shows the Doppler broadened absorption profile of Rubidium (due to reference beam only). Here the stronger absorption is due to  $^{85}\text{Rb}$ , and the weaker absorption is due to  $^{87}\text{Rb}$ . The  $^{87}\text{Rb}$  line comprises of three  $5^2S_{1/2}(F = 2) \rightarrow 5^2P_{3/2}(F = 1, 2, 3)$  transitions, but these are not resolved and manifest together as one line in the data of Figure 2.5 because of Doppler broadening. When the reference probe beam is blocked and only the overlap probe beam is allowed to strike its photodiode, there appear dips in the spectral lines shown in Figure 2.6. For ground state  $F_g$  of each isotope, three transitions  $F_g \rightarrow F_e = F_g, F_g \pm 1$  are resolved and so called cross over resonances are observed midway between each resonance [73]. In this manner, it is possible to obtain 24 atomic resonances. The depth of velocity-selective hole-burning differing for each transition depends on the absorption cross-section for the transition.

The two photodiodes in Figure 2.4 are wired so that their signals subtract by using difference amplifier. If none of the probe beams is blocked, the signals shown in Figure 2.5 and Figure 2.6 are subtracted and the resulting signal is like that in Figure 2.7. In Figure 2.8, a section of spectrum is shown which corresponds to  $5^2S_{1/2}(F = 2) \rightarrow 5^2P_{3/2}(F = 1, 2, 3)$  for  $^{87}\text{Rb}$ . The three peaks labelled as  $R_\mu$  correspond to real transitions from  $F_g \rightarrow F_\mu = \mu$  and  $CO_{\mu\nu}$  are crossover lines between the transitions  $F_g \rightarrow F_\mu = \mu$  and  $F_g \rightarrow F_\nu = \nu$ .

**Width of spectral holes** - As seen in Figure 2.5 and Figure 2.6, width of spectral holes burnt can be order of magnitude narrower than the Doppler broadened absorption lines. The width of these spectral holes is determined by several factors. First, there is an inherent natural line width because of the uncertainty principle, the transition linewidth for  $^{87}\text{Rb}$  ( $F_g = 2 \rightarrow F_e = 3$ ) is about 6 MHz. Secondly, collisions of Rubidium atoms with the walls of the cells and other rubidium atoms broaden the width of spectral holes. Thirdly, the spectral width of the laser is a finite quantity, and the absorption spectra will reflect the laser line width. The linewidth of laser used for this experiment is  $< 1$  MHz.

## 2.7 Polarization Doppler Free Spectroscopy

The spectrum obtained from saturation absorption spectroscopy discussed above subsection 2.6.2 arises as a result of a decrease in the absorption of the probe beam caused by a pump wave that has selectively reduced the population of absorbing level [36]. However, in polarization doppler free spectroscopy [2], the pump wave causes a change in the absorption coefficient  $\alpha$  and a change in refractive index  $n$ . The signals in the latter arise due to the change in the probe wave's polarization state induced by a polarized pump wave [5].

### 2.7.1 Theory

The main principle of polarization doppler free spectroscopy is to induce birefringence in a medium with a circularly polarized pump beam with stronger intensity and probe this with a counterpropagating weak beam having intensity much lower than the saturation intensity of the transition under study. [5]. Consider that the laser is tuned to an allowed transition ( $F \rightarrow F'$ ), where  $F$  and  $F'$  are angular momentum vectors corresponding to ground and excited state respectively. The projection of  $F$  onto the direction of light propagation is represented by  $m_F$ . This  $m_F$  follows different selection rules for different polarized states of laser beam. The  $\Delta m_F = +1$  transitions among magnetic sublevels are excited by right circularly polarized light whereas left circularly polarized light follows the selection rule  $\Delta m_F = -1$ . When light propagation direction is along  $z$ -axis, linearly polarized laser light follows the selection rule  $\Delta m_F = \pm 1$ . Initially all atoms in the medium are in ground state and right circular polarized pump beam traverses through the sample. In the Figure 2.9, it can be seen that the right circularly polarized light excites only  $\Delta m_F = +1$  transitions. The  $\Delta m_F = -1$  and  $\Delta m_F = 0$  transitions are

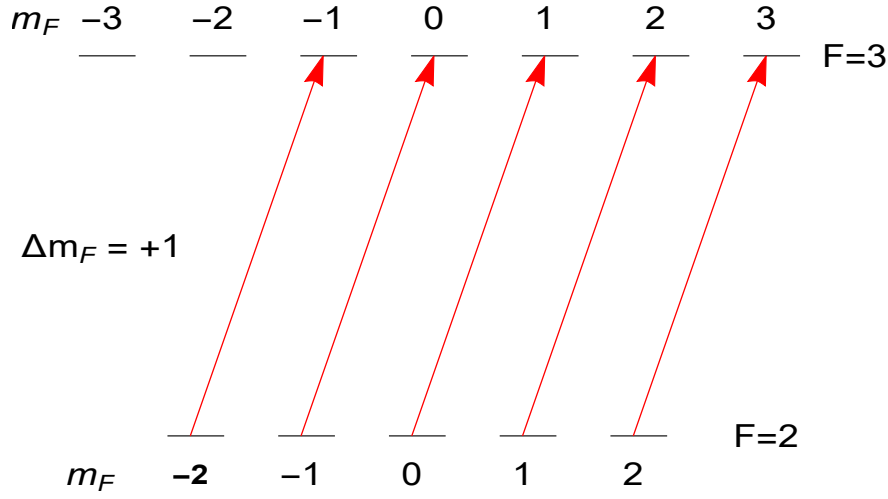


**Figure 2.9:** Transitions induced by  $\sigma^+$  pump beam.

suppressed in this case. Consequently, magnetic sublevels  $m_F = -3$  and  $m_F = -2$  are not populated. This process results in an unequal saturation by the pump beam and therefore, nonuniform population among magnetic sublevels  $m_F$  is established [36]. This non-uniform population is equivalent to an anisotropic distribution of the angular momentum vector  $F$ . Thus, atomic sample becomes birefringent due to right circularly polarized pump beam. A linearly polarized probe beam can be decomposed into two oppositely circular polarized components i.e left circularly polarized and right circularly polarized as given below [5].

$$\mathbf{E} = \mathbf{E}_o e^{i(\omega t - kz)}, \mathbf{E}_o = (E_o, 0, 0) \quad (2.28)$$

with  $\mathbf{E} = \mathbf{E}^+ + \mathbf{E}^-$ , where

$$E^+ = E_o^+ e^{i(\omega t - k^+ z)}, E_o^+ = \frac{1}{2}(\hat{\mathbf{x}} + i\hat{\mathbf{y}}) \quad (2.29)$$

$$E^- = E_o^- e^{i(\omega t - k^- z)}, E_o^- = \frac{1}{2}(\hat{\mathbf{x}} - i\hat{\mathbf{y}}) \quad (2.30)$$

These two components experience different absorption after passing through the birefringent sample. The left hand circularly polarized component undergoes stronger absorption than right circularly polarized part. As a result, these components experience different refractive index. Thus, the plane of polarization of the probe wave is rotated after having

passed through the sample.

Similarly, if the pump beam is left circularly polarized, it will excite  $\Delta m_F = -1$  transitions. For this polarization of pump beam,  $\Delta m_F = +1$  and  $\Delta m_F = 0$  transitions are suppressed as shown in Figure 2.10. Here, the right circularly polarized component of probe beam will experience more absorption and again the plane of polarization of probe wave is rotated.

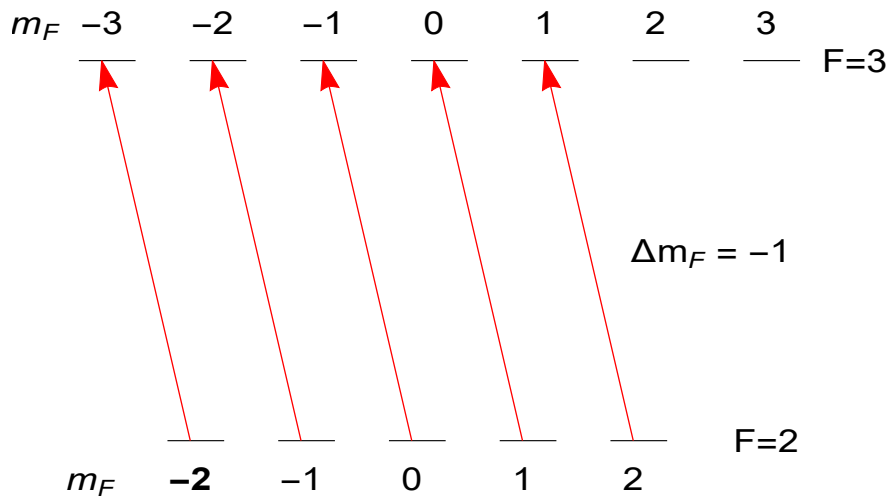


**Figure 2.10:** Transitions induced by  $\sigma^-$  pump beam.

The fact that only a certain group of atoms would experience this non-isotropic orientation must be noted. When frequency of laser is different from the atomic resonant frequency, pump and probe beams interact with the different velocity group of atoms. In this case, probe beam will remain unaffected by the pump beam. For probe beam to experience birefringence, it should interact with the atoms already excited by the pump beam. This happens for the velocity group of atoms [28]:

$$v_z \pm \Delta v_z = \frac{\omega - \omega_0}{k} \pm \frac{\Gamma}{k} \quad (2.31)$$

where  $\Gamma$  is the homogenous linewidth of the considered transition and  $k = k_z$ . This subgroup of atoms will absorb both pump and probe beams. The probe beam's plane of polarization will be rotated after interacting with these velocity group.

So far, we have discussed polarization doppler free spectroscopy qualitatively. In the discussion that follows, we will have a quantitative look at the polarization doppler free spectroscopy. A rubidium cell is illuminated by the pump beam along the  $-z$ -direction.

The probe beam ( $\hat{x} \cos(\phi) + \hat{y} \sin(\phi)$ ) is slightly tilted by an angle  $\phi$  with respect to  $x$ -axis and is allowed to travel along the  $z$ -direction. This probe beam is linearly polarized with  $\phi \simeq \frac{\pi}{4}$ . The resultant electric field of the probe wave after passing through the medium is given by [37]:

$$\vec{E} = \frac{E_0}{\sqrt{2}} \left[ \frac{\hat{x} + i\hat{y}}{\sqrt{2}} e^{(-\alpha_+ L/2)} e^{i(kn_+ L - \phi)} e^{ikL(a_+ + ib_+)} + \frac{\hat{x} - i\hat{y}}{\sqrt{2}} e^{(-\alpha_- L/2)} e^{i(kn_- L + \phi)} e^{ikL(a_- + ib_-)} \right] \quad (2.32)$$

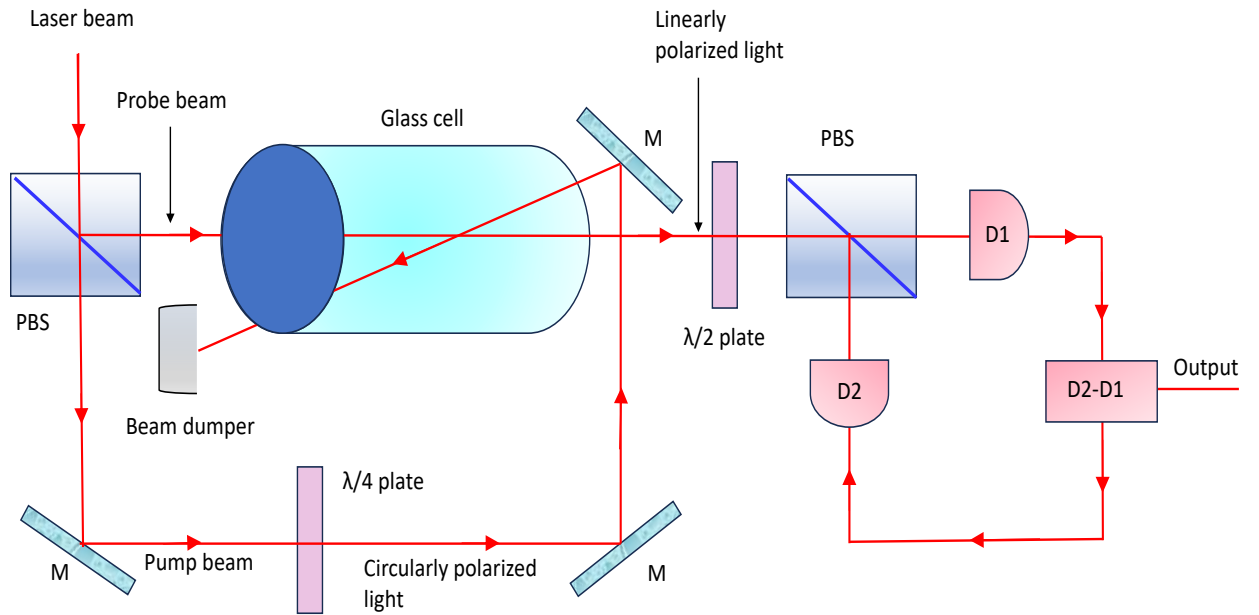


**Figure 2.11:** Experimental setup for polarization doppler free spectroscopy: Polarization Beam Splitter (PBS); Mirror (M); Photodiode ( $D_1$  and  $D_2$ ); Quarter wave plate ( $\lambda/4$ ); Half wave plate ( $\lambda/2$ )

where  $n_+$  and  $n_-$  are the refractive indices of the rubidium vapor for two oppositely circularly polarized components of probe beam and  $\alpha_{\pm}$  is the absorption coefficient for the respective components of the probe wave. The index of refraction for the windows of the absorption cell is a complex quantity  $a_{\pm} + ib_{\pm}$  and is different for  $\sigma^{\pm}$  component of the probe beam and  $k$  is the wave vector. Separating the  $x$  and  $y$  component of electric field,

we have

$$E_x = \frac{E_0}{2\sqrt{2}} [e^{-\alpha_+ L/2} e^{i(kn_+ L - \phi)} e^{ikL(a_+ + ib_+)} + e^{(-\alpha_- L/2)} e^{i(kn_- L + \phi)} e^{ikL(a_- + ib_-)}] \quad (2.33)$$

$$E_y = i \frac{E_0}{2\sqrt{2}} [e^{-\alpha_+ L/2} e^{i(kn_+ L - \phi)} e^{ikL(a_+ + ib_+)} + e^{(-\alpha_- L/2)} e^{i(kn_- L + \phi)} e^{ikL(a_- + ib_-)}] \quad (2.34)$$

The transmitted intensity is  $I_x = c\epsilon_0 E_x E_x^*$ . Let's first compute  $E_x E_x^*$ :

$$E_x E_x^* = \frac{E_0}{8} \left[ e^{-\alpha_+ L} e^{-2klb_+} + e^{-(\alpha_+ \alpha_-) L/2} e^{-2i\phi} e^{ik(n_+ - n_-) L} e^{ikL(a_+ - a_-)} e^{-kl(b_+ + b_-)} \right] \quad (2.35)$$

$$+ e^{(\alpha_+ \alpha_-) L/2} e^{-ik(n_+ - n_-) L} e^{2i\phi} e^{-ikL(a_+ + a_-)} e^{-kl(b_+ + b_-)} \quad (2.36)$$

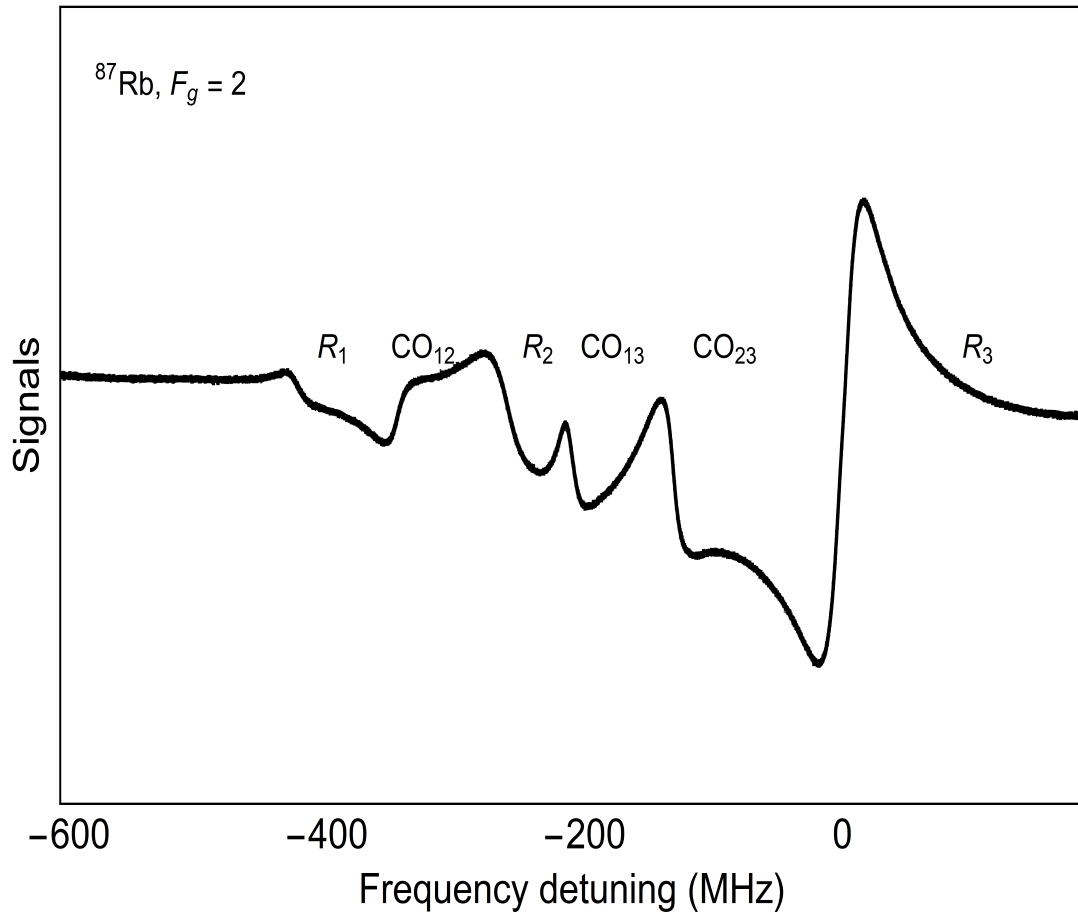


**Figure 2.12:** Polarization spectra for  $F_g = 2 \rightarrow F_e = 1, 2, 3$  transitions in  $^{87}\text{Rb}$

We define average and difference of above mentioned quantities ( $n, a, b, \alpha$ ) as:

$$\begin{aligned} n &= \frac{1}{2}(n_+ + n_-), & \Delta n &= n_+ - n_- \\ a &= \frac{1}{2}(a_+ + a_-), & \Delta a &= a_+ - a_- \end{aligned}$$

$$\begin{aligned} b &= \frac{1}{2}(b_+ + b_-), & \Delta b &= b_+ - b_- \\ \alpha &= \frac{1}{2}(\alpha_+ + \alpha_-), & \Delta \alpha &= \alpha_+ - \alpha_- \end{aligned}$$

Intensity is given by:

$$I_x = c\epsilon_0 E_x E_x^* \quad (2.37)$$

$$= \frac{c\epsilon_0 E_0^2}{8} \left[ e^{-(\alpha + \Delta\alpha/2)} e^{-2kl(b + \Delta b/2)} + e^{\alpha L} e^{-2i\phi} e^{ik\Delta n L} e^{ikL\Delta a} e^{-2kLb} \right] \quad (2.38)$$

$$+ e^{-\alpha L} e^{-iknL} e^{2i\phi} e^{ikL\Delta a} e^{-2kLb} + e^{-\alpha_- L} e^{-2kLb_-} \quad (2.39)$$

Similarly  $I_y$  can be evaluated. The intensity difference between respective components of the probe beam is:

$$\Delta I = I_x - I_y \quad (2.40)$$

$$\Delta I = \frac{c\epsilon_0 E_0^2}{2} \left[ \frac{\pi}{2} - 2\phi + kL(\Delta n + \Delta a) \right] e^{-(\alpha + 2kb)L} \quad (2.41)$$

We can see that signals in polarization doppler free spectroscopy are proportional to the difference in refractive index ( $\Delta n$ ). The refractive index difference calculated for different transitions in the atom will yield polarization spectra.

## 2.7.2 Experimental Setup

The experimental layout of polarization doppler-free spectroscopy used in this experiment is shown in Figure 2.11. In this experiment, a single mode extended cavity diode laser is used. The linewidth of the laser is about  $< 1$  MHz at 780 nm and mode hop free spectral

---

range is 7 – 8 GHz. The output from a single mode extended cavity diode laser is split into a weak probe beam with the intensity much lower than the saturation intensity of the considered transition, and a stronger pump beam with intensity of the order of the saturation intensity. The intensity of pump beam is  $\sim 0.8 \text{ mW/cm}^2$  whereas the intensity of probe beam is  $\sim 20 \text{ }\mu\text{W/cm}^2$ . In this experiment, polarization signals are obtained for the  $D_2$  transition of  $^{87}\text{Rb}$ . A  $\lambda/4$  plate makes the pump beam circularly polarized whereas the probe beam is linearly polarized. The linearly polarized probe beam can be decomposed into two opposite circularly polarized components. These two components experience the same absorption without a pump beam as the sample is isotropic. In the presence of pump beam, these components experience different absorption and different refractive indices yielding polarization spectra. The output signals from the polarizing beam splitter ( $PBS$ ) were focussed onto photodiodes ( $D1$  and  $D2$ ) and were electronically subtracted via the difference amplifier to generate the signals in polarization spectra.

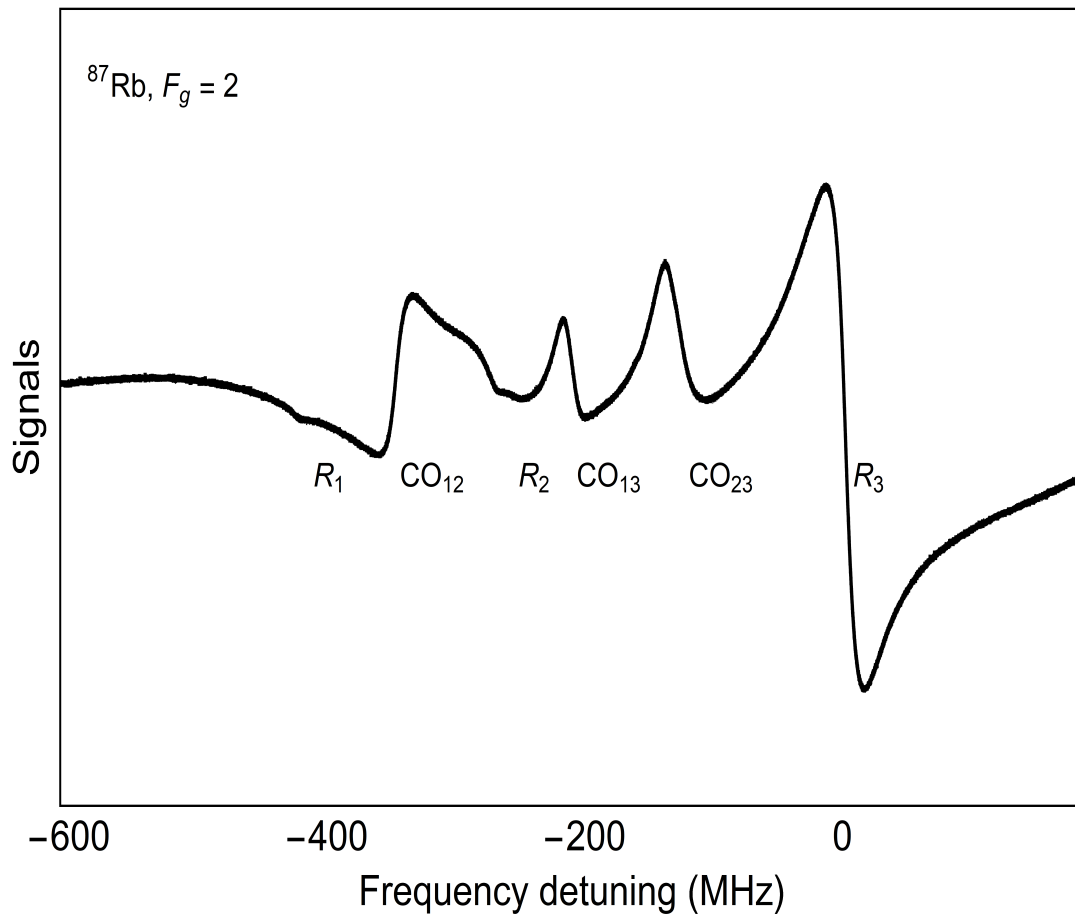


**Figure 2.13:** Polarization spectra for  $F_g = 2 \rightarrow F_e = 1, 2, 3$  transitions in  $^{87}\text{Rb}$ . In this experiment, the circular polarization of the pump beam is opposite to the polarization of the pump beam considered in the experiment of Figure 2.12. By changing the circular polarization, the slope of the polarization signal has reversed.

The spectrum obtained for two opposite circular polarizations of the pump beam is shown in Figure 2.12 and Figure 2.13 respectively. In this spectrum,  $R_1$ ,  $R_2$  and  $R_3$  represent the real transition from  $F_g = 2 \rightarrow F_e = 1$ ,  $F_g = 2 \rightarrow F_e = 2$  and  $F_g = 2 \rightarrow F_e = 3$  respectively. The  $CO_{12}$  corresponds to crossover resonance between  $F_g = 2 \rightarrow F_e = 1$  and  $F_g = 2 \rightarrow F_e = 2$  transition. Similarly,  $CO_{13}$  and  $CO_{23}$  represent crossover peak between  $F_g = 2 \rightarrow F_e = 1$  and  $F_g = 2 \rightarrow F_e = 3$ ,  $F_g = 2 \rightarrow F_e = 2$  and  $F_g = 2 \rightarrow F_e = 3$  transition respectively. It is important to note that opposite circular polarization of pump beam with respect to the experiment of Figure 2.12, has reversed the slope of polarization signal. On comparing this polarization spectra with saturated absorption spectra, we see here that the signal is the first derivative of absorption profile obtained by saturated

absorption spectroscopy. These signals [74] have steep slopes which are used in laser frequency stabilization [40].

<b>Parameter</b>	<b>Experiment Figure 2.12</b>	<b>Experiment Figure 2.13</b>
Intensity of pump laser	0.5 mW/cm <sup>2</sup>	0.5 mW/cm <sup>2</sup>
Intensity of probe laser	60 μW/cm <sup>2</sup>	60 μW/cm <sup>2</sup>
Polarization of probe laser	Linear (+45°)	Linear (+45°)
Polarization of pump laser	Right circular	Left circular

## 2.8 Conclusion

This chapter aimed to explain the fine and hyperfine structure effects resulting in splitting of energy levels in <sup>87</sup>Rb and <sup>85</sup>Rb. It was discussed that the origin of fine structure is due to coupling of electron's spin magnetic moment with the magnetic field of proton. These fine energy levels additionally split into hyperfine energy levels which is a result of an interaction of electromagnetic field produced by the electrons at the nucleus with the electromagnetic multipole moments possessed by the nucleus. The transitions between fine and hyperfine energy levels were resolved using saturated absorption spectroscopy set up. The setup for polarisation spectroscopy, which generates signals for frequency locking was also explained in this chapter. The results shown in this chapter are essential to perform the Imaging experiment described in chapter 4 : Sub tomographic imaging of a birefringent phase pattern localized in a phase space.



# Chapter 3

## 3D Tomographic Imaging in Phase Space

### 3.1 Introduction

In this chapter, we are going to introduce the entirely new concept of classical imaging [1]. It is known that in conventional imaging experiments, optically responsive objects in position space can be imaged using a lens and hence viewed by the human eye. The work described in this chapter goes beyond this usual imaging in position space and explains the concept of imaging phase space patterns. The pattern in phase space cannot be imaged with a lens conventionally and cannot be seen by the human eye. It will be explained in the following sections how a stationary structural pattern can be created from object transparencies and imprinted onto the phase space of an atomic gaseous medium at room temperature. The experiment is based on the concept of velocity selective hole burning in the Doppler broadened absorption profile of an atomic gaseous medium.

### 3.2 Velocity Selective Hole Burning

Let's suppose there is an ensemble of atoms having atomic states  $|\alpha\rangle$  and  $|\beta\rangle$ . The energy separation between these states is  $E_\alpha - E_\beta = \hbar\omega_0$ . The atom is allowed to transit between these two energy levels as per selection rules. It is convenient to represent this atomic

system of two energy levels by a  $2 \times 2$  density matrix [17] :

$$\sigma(z, t, v) = \begin{bmatrix} \sigma_{\alpha\alpha} & \sigma_{\alpha\beta} \\ \sigma_{\beta\alpha} & \sigma_{\beta\beta} \end{bmatrix} \quad (3.1)$$

here  $\sigma_{\alpha\alpha}$  and  $\sigma_{\beta\beta}$  represent population of excited and ground state respectively. The off-diagonal elements are proportional to atomic dipole moment. The number density of atoms is  $N$ . At room temperature, atoms in medium are in continuous random thermal motion. Consequently, there will be distribution of velocities in this ensemble and the same is represented by Maxwellian velocity distribution [17]:

$$N(v_z)dv_z = \sqrt{\frac{m}{2\pi K_B T}} e^{-\frac{mv_z^2}{2K_B T}} dv_z \quad (3.2)$$

The energy levels  $|\alpha\rangle$  and  $|\beta\rangle$  decay with rate constant  $\gamma_\alpha$  and  $\gamma_\beta$  whereas  $\gamma_{\alpha\beta}$  corresponds to the decay rate of atomic dipole moment. The irradiation of the medium to the light will cause the atoms to transit between two energy levels. The excitation process is velocity dependent and excites the atoms to levels  $|\alpha\rangle$  and  $|\beta\rangle$  at excitation rate of  $\lambda_\alpha$  and  $\lambda_\beta$  respectively. Thus, excitation rates of levels  $|\alpha\rangle$  and  $|\beta\rangle$  can be supposed to be of the form:

$$\lambda_j(v_z) = \Lambda_j N(v_z) \quad (j = \alpha, \beta) \quad (3.3)$$

The variation of population of levels with time is dependent on excitation ( $E$ ) and relaxation ( $R$ ) rates and can expressed in the following form [17]:

$$\left( \frac{d\sigma_{\alpha\alpha}}{dt}(z, t, v) \right)_{E+R} = \lambda_\alpha(v) - \gamma_\alpha \sigma_{\alpha\alpha}(z, t, v) \quad (3.4)$$

$$\left( \frac{d\sigma_{\beta\beta}}{dt}(z, t, v) \right)_{E+R} = \lambda_\beta(v) - \gamma_\beta \sigma_{\beta\beta}(z, t, v) \quad (3.5)$$

$$\left( \frac{d\sigma_{\alpha\beta}}{dt}(z, t, v) \right)_{E+R} = -\gamma_{\alpha\beta} \sigma_{\alpha\beta}(z, t, v) \quad (3.6)$$

The population difference under the only action of excitation and relaxation process [ $\frac{d\sigma}{dt} = 0$ ] is thus written as:

$$\sigma_{\alpha\alpha} - \sigma_{\beta\beta} = \left( \frac{\Lambda_\alpha}{\gamma_\alpha} - \frac{\Lambda_\beta}{\gamma_\beta} \right) N(v_z) = P_0 N(v_z) \quad (3.7)$$

where  $P_0 = \left( \frac{\Lambda_\alpha}{\gamma_\alpha} - \frac{\Lambda_\beta}{\gamma_\beta} \right)$  is the total population difference at equilibrium per unit length of the cell. The atomic system mentioned above is made to interact with an electromagnetic wave propagating along  $z$ -axis, the electromagnetic field of this wave is given by:

$$E = E_0 \cos(\omega t - kz) \quad (3.8)$$

where  $\omega$  is the frequency of the field. The combined Hamiltonian of the atomic system and the electromagnetic field is given by:

$$H = H_0 - PE \quad (3.9)$$

where  $H_0$  is the Hamiltonian of the atom in the absence of field and is represented by  $H_0 = \frac{\hbar\omega_0}{2} \begin{pmatrix} 1 & 0 \\ 0 & -1 \end{pmatrix}$ ,  $P$  is the  $x$ - component of the atomic dipole moment. This operator has only off-diagonal matrix elements which can be written as  $\langle \alpha | P | \beta \rangle = \langle \beta | P | \alpha \rangle = \wp$

$$H = \frac{\hbar\omega_0}{2} \begin{pmatrix} 1 & 0 \\ 0 & -1 \end{pmatrix} - \wp E_0 \cos(\omega t - kz) \begin{pmatrix} 0 & 1 \\ 1 & 0 \end{pmatrix} \quad (3.10)$$

Applying rotating wave approximation as  $\omega$  is very close to the atomic frequency  $\omega_0$ . Then

$$H \approx \frac{\hbar\omega_0}{2} \begin{pmatrix} 1 & 0 \\ 0 & -1 \end{pmatrix} - \frac{\wp E_0}{2} \begin{pmatrix} 0 & e^{-i(\omega t - kz)} \\ e^{i(\omega t - kz)} & 0 \end{pmatrix} \quad (3.11)$$

The total time variation of the density matrix is obtained by adding contributions due to excitation, relaxation and the action of em fields:

$$\frac{d\sigma}{dt} = \left( \frac{d\sigma}{dt} \right)_{e+r} - \frac{i}{\hbar} [H, \sigma] \quad (3.12)$$

where  $[H, \sigma] = H\sigma - \sigma H$ . Here time derivative  $\frac{d}{dt}$  is a total time derivative along the path of the atoms moving with velocity  $v$ , so it is replaced by  $\frac{\partial}{\partial t} + v \frac{\partial}{\partial z}$ . Then we have [89, 90]

$$\left( \frac{\partial}{\partial t} + v \frac{\partial}{\partial z} \right) \sigma_{\alpha\alpha} = \lambda_\alpha - \gamma_\alpha \sigma_{\alpha\alpha} - \frac{i\wp\epsilon}{2\hbar} (\sigma_{\alpha\beta} e^{i(\omega t - kz)} - \sigma_{\beta\alpha} e^{-i(\omega t - kz)}) \quad (3.13)$$

$$\left( \frac{\partial}{\partial t} + v \frac{\partial}{\partial z} \right) \sigma_{\beta\beta} = \lambda_\beta - \gamma_\beta \sigma_{\beta\beta} + \frac{i\wp\epsilon}{2\hbar} (\sigma_{\alpha\beta} e^{i(\omega t - kz)} - \sigma_{\beta\alpha} e^{-i(\omega t - kz)}) \quad (3.14)$$

$$\left( \frac{\partial}{\partial t} + v \frac{\partial}{\partial z} \right) \sigma_{\alpha\beta} = -(\gamma_{\alpha\beta} + i\omega_0) \sigma_{\alpha\beta} - \frac{i\wp\epsilon}{2\hbar} (\sigma_{\alpha\alpha} - \sigma_{\beta\beta}) e^{-i(\omega t - kz)} \quad (3.15)$$

For a steady state solution, form is given by  $\sigma_{\alpha\alpha} = n_{\alpha 0}$ ,  $\sigma_{\beta\beta} = n_{\beta 0}$  and  $\sigma_{\alpha\beta} = \rho_0 e^{-i(\omega t - kz)}$ . Thus, we obtain [17]

$$n_{\alpha 0} - n_{\beta 0} = P_0 N(v_z) \left[ 1 - \frac{S^2 \gamma_{\alpha\beta}^2}{\gamma_{\alpha\beta}^2 + (\omega_0 - \omega + kv)^2 + S^2 \gamma_{\alpha\beta}^2} \right] \quad (3.16)$$

Here  $\frac{\varphi^2 E_0^2}{\gamma \gamma_{ab} \hbar^2} = S^2$  is a dimensionless quantity called saturation parameter. Equation 3.16 shows that the population difference as a function of velocity follows the maxwellian distribution  $N(v_z)$ , with an additional minimum when the resonance condition ( $\omega - kv = \omega_0$ ) is fulfilled. The minimum corresponds to the **hole** burnt into the population difference by the travelling wave [3]. In other words, we can say that when a strong monochromatic light at frequency  $\omega$  is incident, the population of the lower state is reduced at the velocity component of  $v = (\omega - \omega_0)/k$ , whereas that of the upper state is raised. Thus, incident light burns a hole in the velocity distribution of the lower state and piles up a peak in that of the upper state. This dip, can, however, be detected if two lasers are used: One beam is saturating pump laser with the wave vector  $k_1$ , which is kept at the frequency  $\omega_1$  and which burns a hole into the velocity class  $v_z + \Delta v_z/2$  with  $v_z = (\omega_0 - \omega_1)/k$  and the other one is a weak probe laser with the wave vector  $k_2$  and a frequency  $\omega$  tunable across the Doppler broadened profile. This probe laser will not cause extra saturation as it is sufficiently weak [5].

### 3.3 Phase Space Imaging Based on Velocity Selective Hole-Burning

#### 3.3.1 Theory

Consider a linearly polarized object laser beam of frequency  $\nu_p$  with transverse intensity profile  $I_p(x, y, \nu_p)$  travelling in an atomic gaseous medium in a direction opposite to the  $z$ -axis as shown in Figure 3.2. The intensity profile  $I_p(x, y, \nu_p)$  represents a  $2D$  image of an object in position space. This object laser beam is allowed to pass through an atomic gaseous medium of length  $L$  where an isolated stationary atom has a ground quantum state  $|g\rangle$  of energy  $E_g$  and an excited quantum state  $|e\rangle$  of energy  $E_e$  with linewidth  $\Gamma$ . The object laser beam is on resonance with a velocity class of atoms of  $z$ -component of

### 3.3. PHASE SPACE IMAGING BASED ON VELOCITY SELECTIVE HOLE- 47 BURNING

---

their velocity equals to [1]

$$v_r = \frac{2\pi(\nu_0 - \nu_p)}{k} \quad (3.17)$$

where  $\nu_0 = \frac{(E_e - E_g)}{h}$  is the resonant frequency,  $k = \frac{2\pi}{\lambda}$  is the magnitude of the propagation vector of the object laser beam having wavelength  $\lambda$ . Owing to the Doppler effect, atoms of other velocity groups are out of resonance. The transverse Doppler shift is negligible due to the nonrelativistic velocity regime at room temperature.

Suppose  $n$  is the number of atoms per unit volume of the gaseous medium. According to Maxwell-velocity distribution, a fraction of atoms with velocity in an interval  $dv_z$  around  $v_z$  at temperature  $T$  is

$$N(v_z)dv_z = \sqrt{\frac{m}{2\pi K_B T}} e^{-\frac{mv_z^2}{2K_B T}} dv_z \quad (3.18)$$

where  $K_B$  is the Boltzmann constant and  $m$  is the mass of an atom. In the presence of an object laser beam, the ground state atoms of resonant velocity class are pumped to the excited state. This results in a steady state difference of atomic number densities in the ground state ( $n_1$ ) and the excited state ( $n_2$ ) at  $v_z$ :

$$n_1(x, y, v_z) - n_2(x, y, v_z) = \frac{nN(v_z)}{1 + \frac{I_p}{I_s} \frac{\Gamma^2}{4[(2\pi\nu_p - 2\pi\nu_0 + kv_z)^2 + \frac{\Gamma^2}{4}]} \quad (3.19)$$

where  $I_s$  is the saturation intensity of atomic transition. The transverse intensity profile  $I_p(x, y, \nu_p)$  of the object laser beam is imprinted in the form of an atomic population difference if attenuation and diffraction of the object laser beam are insignificant. The intensity profile of object laser beam corresponds to a tomograph in the subspace of phase space.

As atoms are uniformly distributed in the position space, the imprinted pattern is delocalized in the direction of propagation of the object laser beam in a 3D position space. In a 3D momentum space, each tomogram is delocalized in all planes parallel to  $p_x - p_y$  plane, where  $p_x$  and  $p_y$  are the  $x$  and  $y$ - components of momentum of an atom. The pattern, on the other hand, is localized in a unique 3D subspace spanned by  $\hat{x}$ ,  $\hat{y}$  and  $\hat{p}_z$  coordinates where  $\hat{p}_z$  is the  $z$  component of momentum of atoms. When three overlapping object laser beams with the same linear polarization but distinct intensity profiles and frequencies pass through the atomic medium, each beam imprints a different pattern in different velocity group. These patterns are located at different  $p_z$  corresponding to the resonating velocity class of atoms addressed by the resonating object laser beam. As a

result, a localized pattern of all position space objects is imprinted onto a 3D subspace of the 6D phase space of atoms as shown in Figure 3.1.

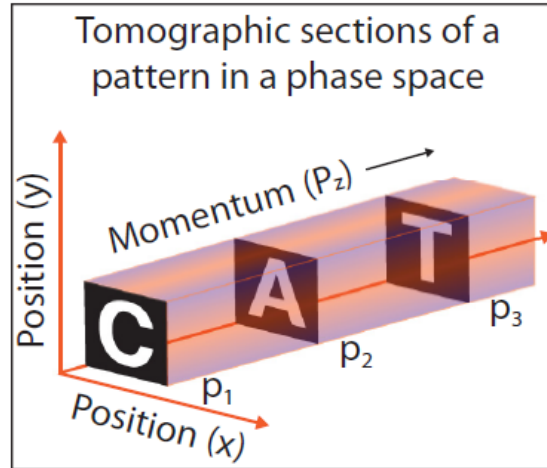


**Figure 3.1:** A pattern localized in a 3D phase space and its three tomograms [1].

To image such a pattern, a counterpropagating linearly polarized imaging laser beam of frequency  $\nu_r$  is overlapped with the object laser beams travelling through the atomic gaseous medium. The total absorption coefficient  $\alpha$  of the imaging laser beam is [17]

$$\alpha(x, y, \delta\nu) = \int_{-\infty}^{\infty} [n_1(x, y, v_z) - n_2(x, y, v_z)] \sigma_o \left( \frac{\frac{\Gamma^2}{4}}{(2\pi\delta\nu - kv_z)^2 + \frac{\Gamma^2}{4}} \right) dv_z \quad (3.20)$$

where  $\sigma_o$  is the peak absorption crosssection of the atomic transition and  $\delta\nu = \nu_r - \nu_0$  is the frequency detuning. If the imaging laser beam interacts with a velocity class of atoms excited by object laser beams, its absorption reduces. This produces velocity selective hole burning in the Doppler broadened absorption profile of the atomic medium. For the incident transverse intensity profile of the imaging laser beam  $I_r(x, y, \delta\nu)$ , the transmitted imaging laser beam intensity profile after passing through the gaseous medium is [1]

$$I_r(x, y, \delta\nu) \exp(-OD(x, y, \delta\nu)) \quad (3.21)$$

where  $OD(x, y, \delta\nu) = \alpha(x, y, \delta\nu)L$  is the optical density of the atomic medium. The optical density profile, at a detuning  $\delta\nu$ , corresponds to a tomographic section of the phase space pattern, at  $p_z = \frac{2\pi m \delta\nu}{k}$ . If object laser beams are present, then optical density

### 3.3. PHASE SPACE IMAGING BASED ON VELOCITY SELECTIVE HOLE- 49 BURNING

of imaging laser beam decreases. A change in the optical density profile in the presence of object laser beams is

$$\Delta OD(x, y, \delta\nu) = -\ln\left(\frac{I_{on}(x, y, \delta\nu)}{I_{off}(x, y, \delta\nu)}\right) \quad (3.22)$$

where  $I_{off}(x, y, \delta\nu)$  is the intensity profile of the imaging laser beam in the absence of object laser beams. This change in the optical density profile represents an image of the tomographic section.

#### 3.3.2 Experimental Setup

##### Imprinting a Pattern in Phase Space

To begin with, object laser beams are passed through Single Mode (SM) polarization maintaining optical fibers. The intensity of object laser beam is  $\sim 2 \text{ mW/cm}^2$ . These fibers act as transverse mode filters and produce beams of a Gaussian transverse intensity profile. The mode-filtered collimated object laser beams of frequencies  $\nu_1$ ,  $\nu_0$  and  $\nu_2$  then travel through mask-1, mask-2 and mask-3, respectively as shown in Figure 3.2 [1].

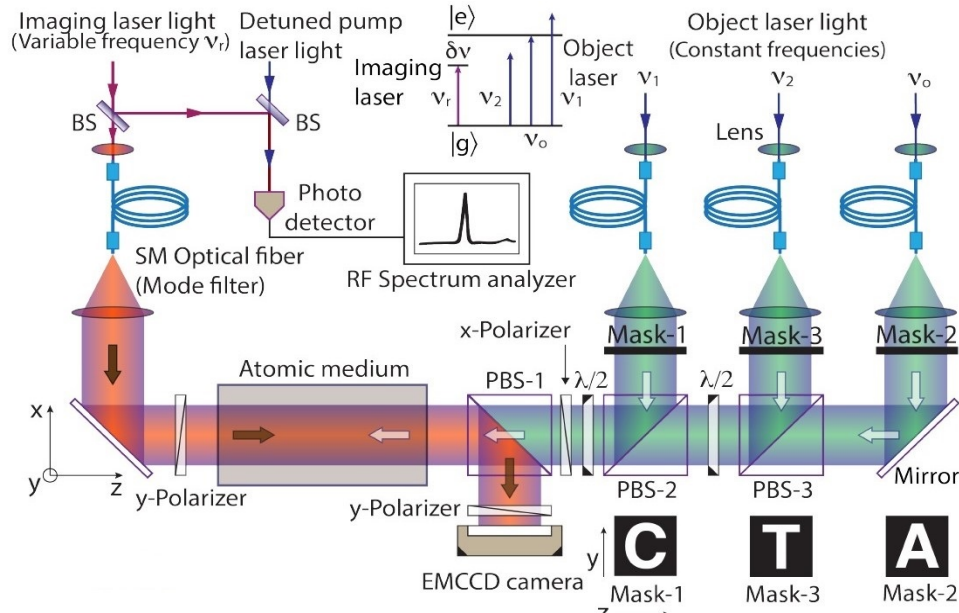


**Figure 3.2:** Experimental schematic diagram [1]

Each mask consists of an image of an alphabet of the English script: C (on mask-1), A (on mask-2), and T (on mask-3). All alphabets are transparent, and the remaining part

### 50 3.3. PHASE SPACE IMAGING BASED ON VELOCITY SELECTIVE HOLE-BURNING

of each mask is entirely opaque to light. The transverse intensity profiles of object laser beams after passing through masks correspond to alphabets C (at  $\nu_1$ ), A (at  $\nu_0$ ) and T (at  $\nu_2$ ).

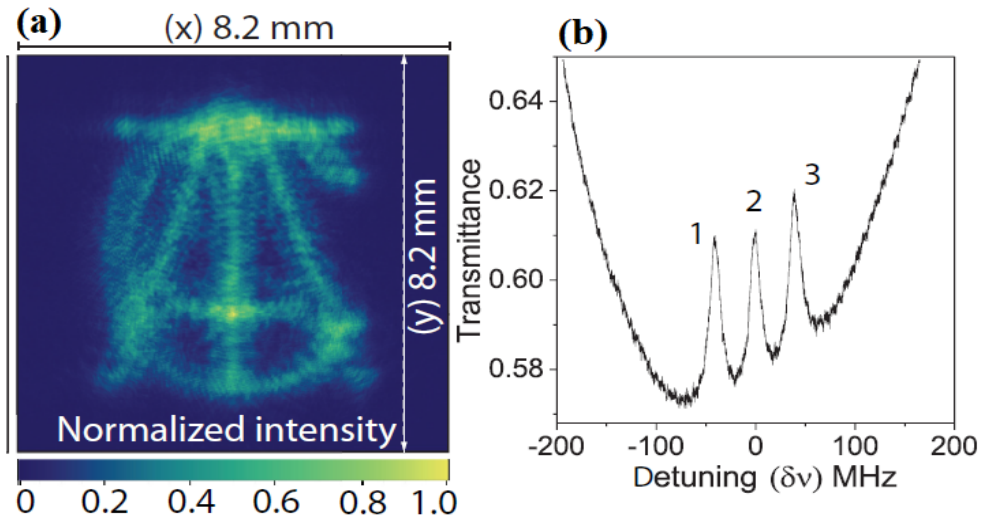


**Figure 3.3:** (a) A 2D transverse intensity profile of the overlapped object laser beams. All three letters overlap with each other [1]. (b) Transmittance, for the imaging laser beam, of the atomic medium in the presence of object laser beams without masks [1].

All three object laser beams are overlapped on polarization beam splitters ( $PBS - 3$ ,  $PBS - 2$ ). The  $x$ -polarizer is placed before  $PBS - 1$  to make these overlapped object laser beams linearly  $x$ -polarized. Before and after the  $PBS - 2$ , two half wave-plates are placed to rotate the linear polarization of the object laser beams to equalize the intensity. Before their entrance into the atomic medium, the image of the transverse intensity profile of the overlapped object laser beams is displayed in Figure 3.3(a), where images of alphabets overlap. The overlapping alphabets are blurred due to diffraction of object laser beams. In Figure 3.2, after  $PBS-1$ , beam color is changed just to show image and object laser beam differently. Both the beams are locked to the same  $D_2$  transition of wavelength  $\lambda = 780$  nm.

An atomic gaseous medium is a 10 cm long rubidium ( $^{87}Rb$ ) vapor cell isolated from an external magnetic field. The Doppler shift generated by atomic motion broadens the linewidth of the resonant transition of the atomic medium. The overlapped object laser beams are then allowed to pass through this atomic medium. An object laser beam of frequency  $\nu_0$  is on resonance to the atomic transition of stationary  $^{87}Rb$  atoms where a ground quantum state is  $5^2S_{1/2}$  with total angular momentum quantum number  $F = 2$

( $|g\rangle$ ), and an excited quantum state is  $5^2P_{3/2}$  with  $F = 3$  ( $|e\rangle$ ). The wavelength of this transition is  $\lambda \simeq 780$  nm for stationary rubidium atoms.

The frequency of object laser beam is stabilized to the atomic transition, and three object laser beams of different frequencies are produced by shifting object laser light frequency with acousto-optic modulators. An object laser beam of frequency  $\nu_0$  is on resonance with an atomic velocity class of  $v_z = 0$  and it imprints an image of an alphabet **A** in this zeroth velocity class in the form of an atomic population difference. An object laser beam of frequency  $\nu_1$  is blue tuned by +40 MHz from the resonant transition for stationary atoms. It is on resonance with atomic velocity class of  $v_z = -31.2$  m s<sup>-1</sup>, and an image of an alphabet **C** is imprinted in this velocity class of atoms. Similarly, object laser beam frequency  $\nu_2$  red detuned by -40 MHz imprints an image of an alphabet **T** in the velocity class  $v_z = +31.2$  m s<sup>-1</sup>.

### Imaging the Phase Space Pattern

The phase-space pattern is imaged with a  $y$ -polarized imaging laser beam passing through the atomic medium in the opposite direction relative to the propagation direction of object laser beams. The image laser beam has a intensity of  $\sim 80$   $\mu$ W/cm<sup>2</sup>. The imaging laser is also frequency locked to the same resonant transition of stationary atoms and its frequency is shifted by acousto-optic modulators. The imaging laser beam is reflected by  $PBS - 1$ , after passing through the atomic medium, and its transverse intensity distribution at different detunings is captured with an electron-multiplying charge coupled device ( $EMCCD$ ) camera without gain multiplication. The object laser beam is extracted and red detuned by 190 MHz from the resonant transition. On a nonpolarization beamsplitter, this extracted object laser light is overlapped with the imaging laser of the same polarization. A quick response photodetector detects the beating signal of two lasers, which is then analysed using a radiofrequency spectrum analyzer, as illustrated in Figure 3.2. The frequency of the beating signal, which corresponds to a frequency difference of two lasers, is used to determine the detuning.

### Capturing Different Tomograms

By varying the frequency of the imaging laser beam, tomograms at different  $p_z$  are imaged. In the presence of object laser beams without masks, the transmittance of the atomic vapor cell for the imaging laser beam, at different detuning  $\delta\nu$ , is shown in Figure 3.3(b). The object laser beams of frequency  $\nu_1$ ,  $\nu_0$ , and  $\nu_2$  generate velocity-selective hole-burning in

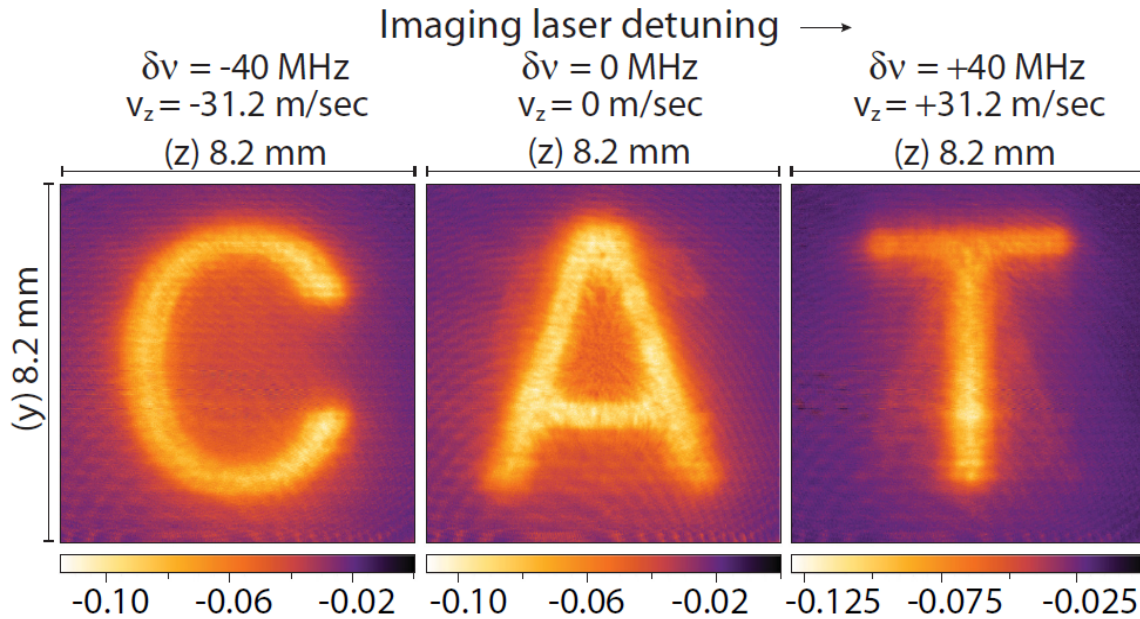


**Figure 3.4:** Three tomographic images of a localized pattern in the 3D phase space captured at different detunings of the imaging laser beam. Each image is a plot of a change in the optical density  $\Delta OD(z, y, \delta\nu)$  [1].

a Doppler-broadened absorption profile, represented by three peaks labelled as 1, 2, and 3, respectively.

The frequency of the imaging laser beam is red detuned by  $\delta\nu = -40 \text{ MHz}$  from the resonant transition. In the absence of three object laser beams, its transverse intensity profile  $I_{off}(x, y, \delta\nu)$  is captured with an EMCCD camera. Then another image of the imaging laser beam intensity  $I_{on}(x, y, \delta\nu)$  is captured in the presence of three object laser beams after a time delay. A change in the optical density profile  $\Delta OD(x, y, \delta\nu)$  is evaluated and tomographic image of a letter *C* is obtained. Before the construction of images, a reflection transformation in a plane parallel to the  $y - z$  is made as imaging laser beam is reflected by *PBS* - 1 and  $\Delta OD(x, y, \delta\nu)$  is transformed to  $\Delta OD(z, y, \delta\nu)$ . Similar measurements are performed for detuning  $\delta\nu = 0 \text{ MHz}$  and  $\delta\nu = +40 \text{ MHz}$  shown in Figure 3.4. By combining all the tomographic images, the word CAT is formed. In contrast to Figure 3.3(a), where non-selective image consists of all letters and it is a direct image of object laser beams, in Figure 3.4, different letters are tomographically selected and imaged selectively in phase space. The Figure 3.4 is a false color plot, it has no connection with wavelength of laser.

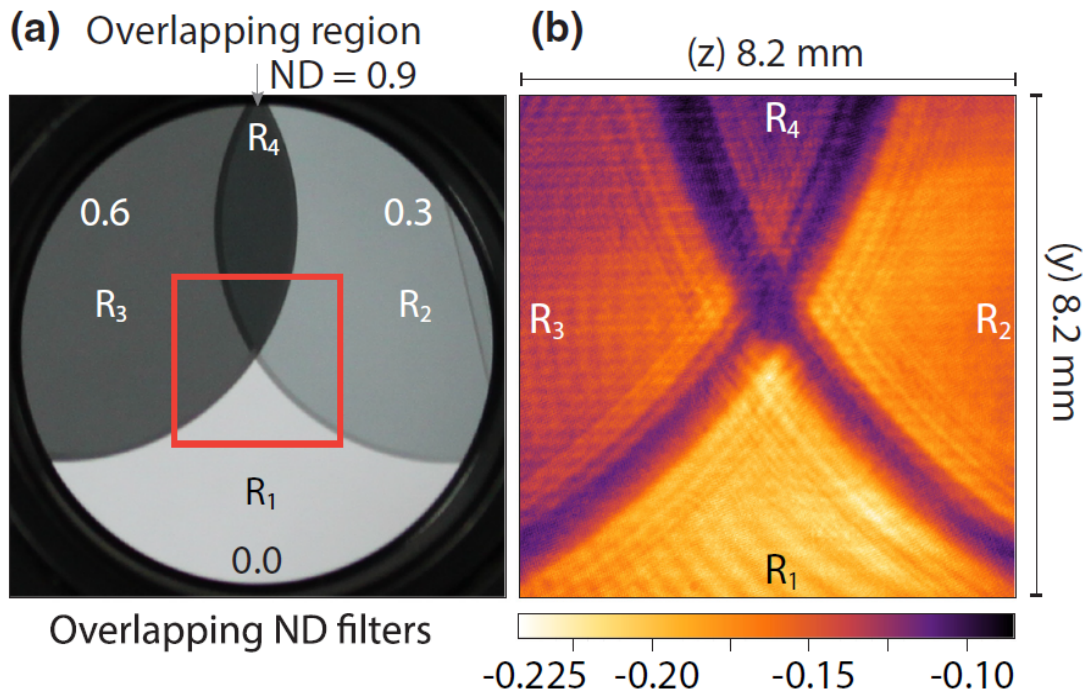


**Figure 3.5:** (a) A photograph of overlapping neutral density filters [1]. An image,  $\Delta OD(z, y, \delta\nu = 0)$ , of an area enclosed by a square as shown in (b) [1].

### Imaging of a Variable Depth Phase-Space Pattern

In another experiment, an object of nonuniform transmittance is imaged using a similar concept. This object with non-uniform transmittance generates a phase space pattern of variable depth. To form this object, two neutral density filters of neutral densities (ND) 0.3 and 0.6 overlap to form four different depth regions, Figure 3.5(a), of this object. These four different are  $R_1$  (ND=0),  $R_2$  (ND=0.3),  $R_3$  (ND=0.6) and  $R_4$  (ND=0.9). The intensity profile of the object laser beam through four regions produces hole-burning of different depths in the absorption profile of the atomic gaseous medium. The object is positioned in place of a mask-2 and image captured with the imaging laser is shown in Figure 3.5(b). The imaging laser beam is on resonant with the velocity class  $v_z = 0$ . It can be seen in Figure 3.5 (b) that the imaging laser beam intensity varies as it passes through the object of non-uniform transmittance and an image of change in optical density  $OD(z, y, \delta\nu = 0)$  of the atomic gaseous medium is constructed.

## 3.4 Conclusion

This is the first experiment in phase space imaging concept which is presented in Ref [1]. This idea is further extended for transparent phase space localized objects which is the main research component of this thesis. It is explained in chapter 4: Sub tomographic imaging of a birefringent phase pattern localized in a phase space.

This newly proposed concept in Ref. [1] was discussed in this chapter. This concept differs from the typical imaging experiment carried out in position space. The experiment to create and image structural patterns in phase space was reported. The object laser beam interacted with the three different position space localized objects and imprinted their tomographic images onto the phase space of atomic medium. In this experiment, objects imaged were three 2D transparent masks. Each mask consisted of an image of an alphabet of the English script: "C", "A", and "T" respectively. All alphabets were transparent, and the remaining part of each mask was entirely opaque to light. The three object laser beams were of different frequencies and addressed different velocity groups in the atomic medium. The pattern is localized in a unique 3D subspace spanned by  $\hat{x}$ ,  $\hat{y}$  and  $\hat{p}_z$  coordinates where  $\hat{p}_z$  is the  $z$  component of momentum of atoms. The three tomographic images of the localized phase space pattern were then captured by a single image laser beam. The frequency of the image laser beam was shifted to capture images at three distinct momentum locations. By combining all the tomographic images, the word CAT is formed. It was explained how this image laser beam never interacted with the actual position space localized objects. The theory behind the experiment's central idea, velocity-selective hole burning was explained. An another experiment was discussed where an object having non-uniform transmittance was imaged using the same concept.

# Chapter 4

## Sub tomographic imaging of a birefringent phase pattern localized in a phase space

### 4.1 Introduction

In this chapter, imprinting and imaging of a transparent birefringent pattern in phase space of Rubidium atoms is explained. Such a transparent birefringent phase pattern changes the phase of transmitted light, which depends on polarization and position of incident light without absorption. A thorough knowledge of imaging the transparent object has been offered by F. Zernike [48–50]. Another scheme to image weakly absorbing materials based on phase contrast method was demonstrated in Ref. [51]. However, these experiments were performed in position space. In this chapter, an experiment conducted to imprint the birefringent phase pattern onto a phase space of an atomic gaseous medium by using atomic state dependent velocity selective hole burning is described. A laser beam of constant frequency, after interaction with a position localized transparent birefringent phase pattern, is passed through a Doppler broadened atomic gaseous medium to imprint the pattern onto a phase space of atoms at room temperature. The pattern is localized in a unique three dimensional subspace of a six-dimensional phase space of atoms. A linearly polarized counter-propagating and overlapping imaging laser beam of variable frequency is detected by a camera after its polarization analysis to construct two sub-tomographs of the imprinted phase space localized pattern.

## 4.2 Transparent Birefringent Phase Pattern Localized in a Position Space

A transparent birefringent phase pattern modifies the phase of transmitted light. It introduces a phase shift  $\Phi_H(x, z)$  in a horizontally polarized ( $\hat{z}$ ) component of transmitted light and  $\Phi_V(x, z)$  in a vertically polarized ( $\hat{x}$ ) component of transmitted light, at an arbitrary location  $(x, z)$  on the pattern. The transmitted electric field of a plane wave propagating along  $y$ -axis, for  $\hat{z}$  polarized component, is  $E_H e^{-i(2\pi\nu_p t - ky)} e^{i\phi_H(x, z)\hat{z}}$ , where  $E_H$  is the electric field amplitude,  $\nu_p$  is frequency,  $k = 2\pi/\lambda$  is the magnitude of propagation vector at wavelength  $\lambda$  and  $\Phi_H(x, z)$  is the phase shift introduced by the pattern. Similarly, the transmitted electric field for  $\hat{x}$  polarized component is  $E_V e^{-i(2\pi\nu_p t - ky)} e^{i\phi_V(x, z)\hat{x}}$ , where  $\Phi_V(x, z)$  is the phase shift introduced by the pattern. If the incident light is linearly polarized such that its plane of polarization is oriented at an angle  $-45^\circ$  *w.r.t.*  $z$ -axis, which is an equal superposition of horizontally and vertically polarized components then the transmitted light exhibits a change in the polarization such that the transmitted electric field is  $E_t e^{-i(2\pi\nu_P t - ky)} e^{i\phi_V(x, z)} (\hat{x} - e^{i\phi(x, z)} \hat{z}) / \sqrt{2}$ . Therefore, a change in polarization depends on the position dependent phase difference given by:

$$\phi(x, z) = \phi_H(x, z) - \phi_V(x, z) \quad (4.1)$$

which is a representation of birefringent property of the transparent polarization sensitive phase pattern localized in  $x$ - $z$  position space. A transparent birefringent phase pattern is shown in Figure 4.1, where the darker region represents the phase difference,  $\phi(x, z) = +\frac{\pi}{2}$  while a lighter region represents  $\phi(x, z) = -\frac{\pi}{2}$ . Therefore, transmitted light just close to the pattern is right circularly polarized corresponding to the darker region and left circularly polarized in the lighter region.

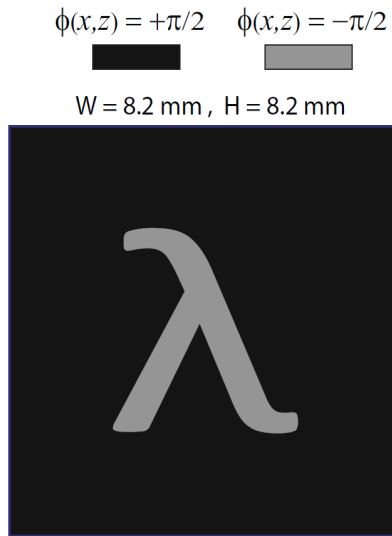


**Figure 4.1:** A position space localized transparent birefringent phase pattern,  $\phi(x, z)$ .

If a camera is used to directly image the transparent birefringent phase pattern, no intensity image is formed. To produce transparent birefringent phase pattern in the experiment performed for this thesis, a linearly polarized light is retro-reflected from a reflection-type *SLM* with plane of polarization of beam oriented at an angle of  $-45^\circ$  *w.r.t.*  $z$ -axis. This pattern is equivalent to a transmission type transparent birefringent phase pattern, where a retro-reflected light exhibits a position and polarization dependent phase shift. The *SLM*'s reflecting surface is kept perpendicular to  $y$ -axis and it introduces a position dependent phase shift in the horizontal polarization component of the incident beam as shown in Figure 4.3, whereas the phase of vertical polarization component is uniformly shifted. This produces the required phase shift  $\phi(x, z)$ . A pattern shown in Figure 4.1 is displayed on *SLM* and transferred to the retro-reflected imprinting laser beam.

### 4.3 Imprinting of a Transparent Birefringent Phase Pattern onto a 3D Phase Space

Consider a linearly polarized laser beam of frequency  $\nu_p$  and transverse intensity profile  $I_p(x, y, \nu_p)$ . This beam interacts with the birefringent phase pattern displayed on *SLM* and is known as imprinting beam. It is allowed to pass through the atomic gaseous medium in a direction opposite to the  $z$ -axis. The electric field of an imprinting laser

beam propagating along  $-z$ -axis is given by

$$\vec{E}_p = E_0 e^{-i(2\pi\nu_P t + kz)} e^{i\phi_V(x,y)} (\hat{x} + e^{i\phi(x,y)} \hat{y}) \quad (4.2)$$

where  $E_0$  is an amplitude of electric field,  $\vec{k}$  is a propagation vector of imprinting laser beam,  $\hat{x}$  and  $\hat{y}$  are the unit vectors representing linear polarization. A position space localized transparent birefringent phase pattern is displayed on *SLM*. As can be seen in Figure 4.3, after reflection by *BS-2*, the birefringent phase pattern is denoted by  $\phi(x, y)$ . Note that after this reflection the direction of propagation of the imprinting laser beam is changed from  $+y$  axis to  $-z$ -axis. Thus, the imprinting laser beam carrying information of the position localized pattern is propagating along  $-z$ -axis in the atomic gaseous medium, where  $z$  axis is considered as a quantization axis. A position space localized pattern is imprinted onto the phase space of atoms by using atomic state dependent velocity selective hole burning in a Doppler broadened atomic gaseous medium.

After imprinting beam interacts with the pattern displayed on *SLM*, some regions on the wavefront where  $\phi(x, y) = +\pi/2$ , imprinting laser beam becomes  $\hat{\sigma}^+$  circularly polarized (left circular polarization). For regions where  $\phi(x, y) = -\pi/2$ , imprinting laser beam becomes  $\hat{\sigma}^-$  circularly polarized (right circular polarization). This  $\sigma$ -polarization convention is defined *w.r.t.* a right-handed coordinate system given in Figure 4.3. Note that after a reflection by *BS - 2* the right circular polarization becomes the left circular polarization and vice-versa, but the  $\sigma$ -polarization convention remains unchanged. This position dependent circular polarization produces an atomic state selective excitation of atoms. If this pattern is imaged on camera, no image is formed as can be seen in Figure 4.2 (b). To transfer this image to phase space of atoms, consider a ground state of an atom  $|F_g, m_F\rangle$  with energy  $E_g$  and an excited state  $|F_e, m'_F\rangle$  with energy  $E_e$ , where magnetic quantum states are labelled by  $m_F$  and  $m'_F$ . Here  $z$ -axis is considered as a quantization axis.

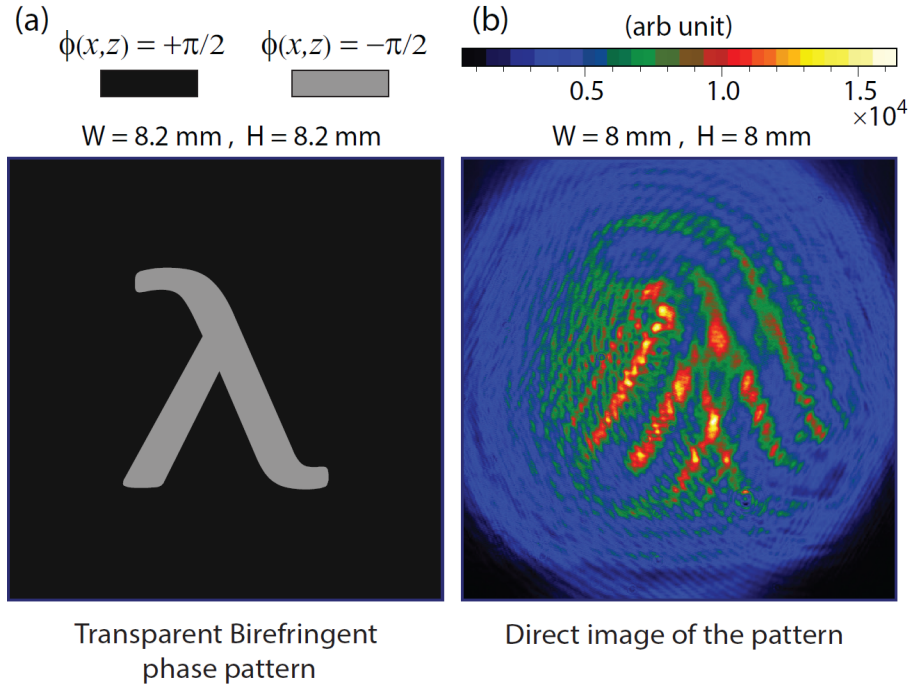


**Figure 4.2:** (a) A position space localized transparent birefringent phase pattern  $\phi(x, z)$ . (b) A transverse intensity profile of the retro-reflected beam measured by a camera-2

For a stationary atom, maximum absorption occurs when frequency of light matches the atomic resonant transition frequency as:

$$\nu_0 = \frac{(E_e - E_g)}{h} \quad (4.3)$$

where  $h$  is the planck's constant. Regions on the wavefront of imprinting laser beam, where beam is  $\hat{\sigma}^+$  polarized, light excites atoms from a ground state  $|F_g, 0\rangle$  to an excited state  $|F_e, +1\rangle$  and regions where beam wavefront is  $\hat{\sigma}^-$  polarized, light excites atoms from  $|F_g, 0\rangle$  to an excited state  $|F_e, -1\rangle$ , considering a single magnetic sub-level of ground state and three magnetic sub-levels of excited state.

60 4.3. IMPRINTING OF A TRANSPARENT BIREFRINGENT PHASE PATTERN ONTO A 3D PHASE SPACE

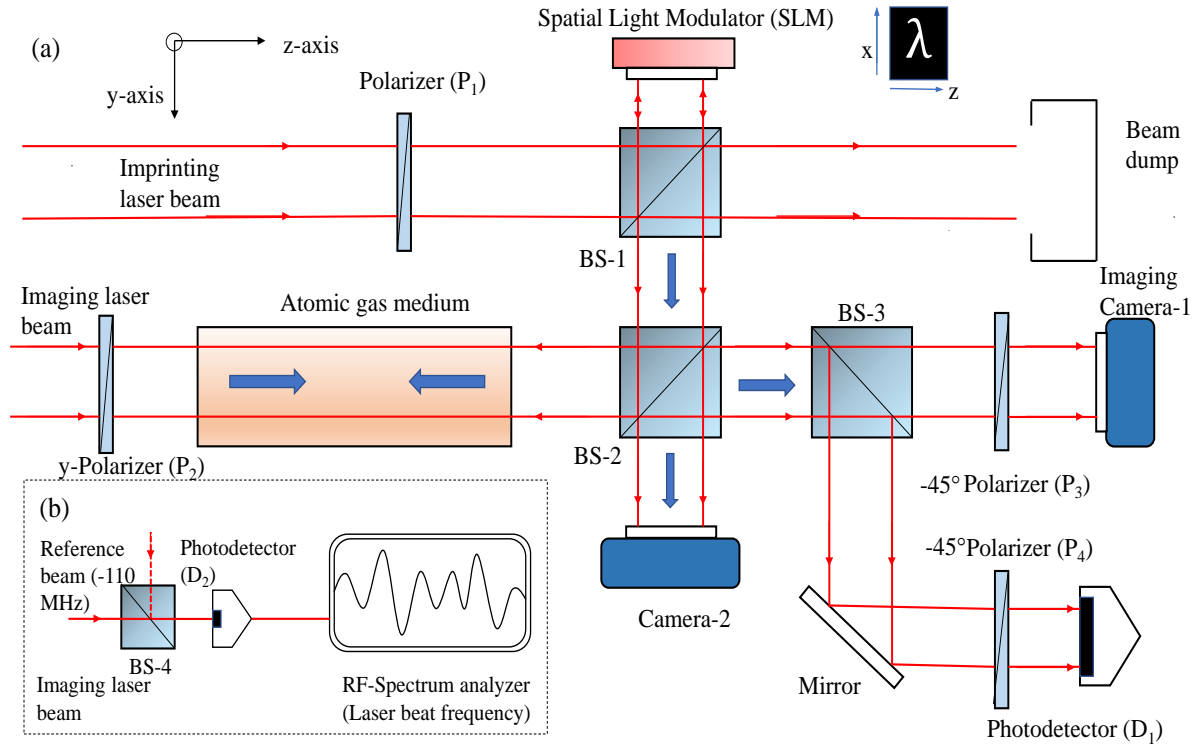


**Figure 4.3:** (a) Experimental schematic diagram of a sub-tomographic imaging experiment (b) part of the experiment to measure frequency difference of lasers by time domain interference on a fast response photodetector

At room temperature, atoms are moving with a Maxwell velocity distribution, therefore, atoms of a particular velocity class  $v_r$  moving along  $z$ -axis are in resonance with the imprinting laser beam because of the Doppler shift, which is given by:

$$v_r = \frac{2\pi(\nu_0 - \nu_P)}{k} \quad (4.4)$$

where  $k = \frac{2\pi}{\lambda}$ ,  $\lambda$  is wavelength of exciting laser beam in a rest frame of reference. Here, atoms moving along a transverse direction to the beam propagation experience a negligible transverse Doppler shift at room temperature. Consider,  $n$  is number of atoms per unit volume at an absolute temperature  $T$ , a fraction of atoms in an interval  $dv_z$  around  $z$ -component of velocity  $v_z$  of atoms is given by the Maxwell velocity distribution

$$f(v_z)dv_z = \sqrt{\frac{m}{2\pi k_B T}} e^{-mv_z^2/2k_B T} dv_z \quad (4.5)$$

where  $k_B$  is the Boltzmann constant and  $m$  is mass of an atom. Imprinting laser beam causes velocity selective and magnetic state selective excitation of atoms. Therefore, for  $\hat{\sigma}^+$  polarized regions, atom number difference per unit volume of atoms in the ground state  $|F_g, 0\rangle$  with atomic density  $n_1(x, y, v_z)$  and in the excited state  $|F_e, +1\rangle$  with atomic density  $n_2^+(x, y, v_z)$  is given by

$$n_1(x, y, v_z) - n_2^+(x, y, v_z) = \frac{nf(v_z)}{1 + \frac{I_p^+(x, y, \nu_p)\Gamma^2}{4I_s^+ \left( (2\pi\nu_p - 2\pi\nu_0 + kv_z)^2 + \Gamma^2/4 \right)}} \quad (4.6)$$

where  $I_s^+$  is the saturation intensity of  $\sigma^+$  atomic transition,  $I_p^+(x, y, \nu_p)$  is the intensity of imprinting laser beam at  $\hat{\sigma}^+$  polarized regions and  $\Gamma$  is the linewidth of transition. Similarly, for  $\hat{\sigma}^-$  polarized regions, atom number difference per unit volume of atoms in the ground state  $|F_g, 0\rangle$  with atomic density  $n_1(x, y, v_z)$  and in the excited state  $|F_e, -1\rangle$  with atomic density  $n_2^-(x, y, v_z)$  is given by:

$$n_1(x, y, v_z) - n_2^-(x, y, v_z) = \frac{nf(v_z)}{1 + \frac{I_p^-(x, y, \nu_p)\Gamma^2}{4I_s^- \left( (2\pi\nu_p - 2\pi\nu_0 + kv_z)^2 + \Gamma^2/4 \right)}} \quad (4.7)$$

where  $I_s^-$  is the saturation intensity of  $\sigma^-$  atomic transition,  $I_p^-(x, y, \nu_p)$  is the intensity of imprinting laser beam at  $\hat{\sigma}^-$  polarized regions. For a uniform beam,  $I_p^+(x, y, \nu_p) = I_p^-(x, y, \nu_p)$ . This magnetic state dependent and velocity selective atomic population difference given by  $n_1(x, y, v_z) - n_2^+(x, y, v_z)$  and  $n_1(x, y, v_z) - n_2^-(x, y, v_z)$  together represents a 3D phase space localized pattern with  $p_z = mv_z$ . In a 3D position space, atoms are randomly moving and an excited atom can be anywhere on  $z$ -axis, therefore, this pattern is delocalized in a 3D position space along  $z$ -axis.

## 4.4 Imaging of a 3D Phase Space Localized Pattern

The imprinted pattern localized in a unique 3D subspace of phase space is imaged tomographically by an another beam known as imaging beam. The horizontally polarized (along  $y$ -axis) imaging beam of uniform intensity  $I_r(x, y, \delta\nu)$  and frequency  $\nu_r$  is counter-propagating w.r.t. imprinting laser beam. This beam is overlapped with the imprinting laser beam and passed through an atomic gaseous medium as shown in Fig. 4.3. A linearly polarized beam is a linear superposition of  $\hat{\sigma}^+$  and  $\hat{\sigma}^-$  circular polarizations.

Therefore, each circular polarization component of the imaging laser beam experiences a different absorption and refractive index at different transverse locations  $(x, y)$  and detunings  $\delta\nu = \nu_r - \nu_0$ , as the medium is excited magnetic state selectively and velocity selectively. A particular location of a tomographic section on a momentum axis is given by:

$$p_z = 2\pi m\delta\nu/k \quad (4.8)$$

which is selected by the frequency detuning  $\delta\nu$  of imaging laser beam.

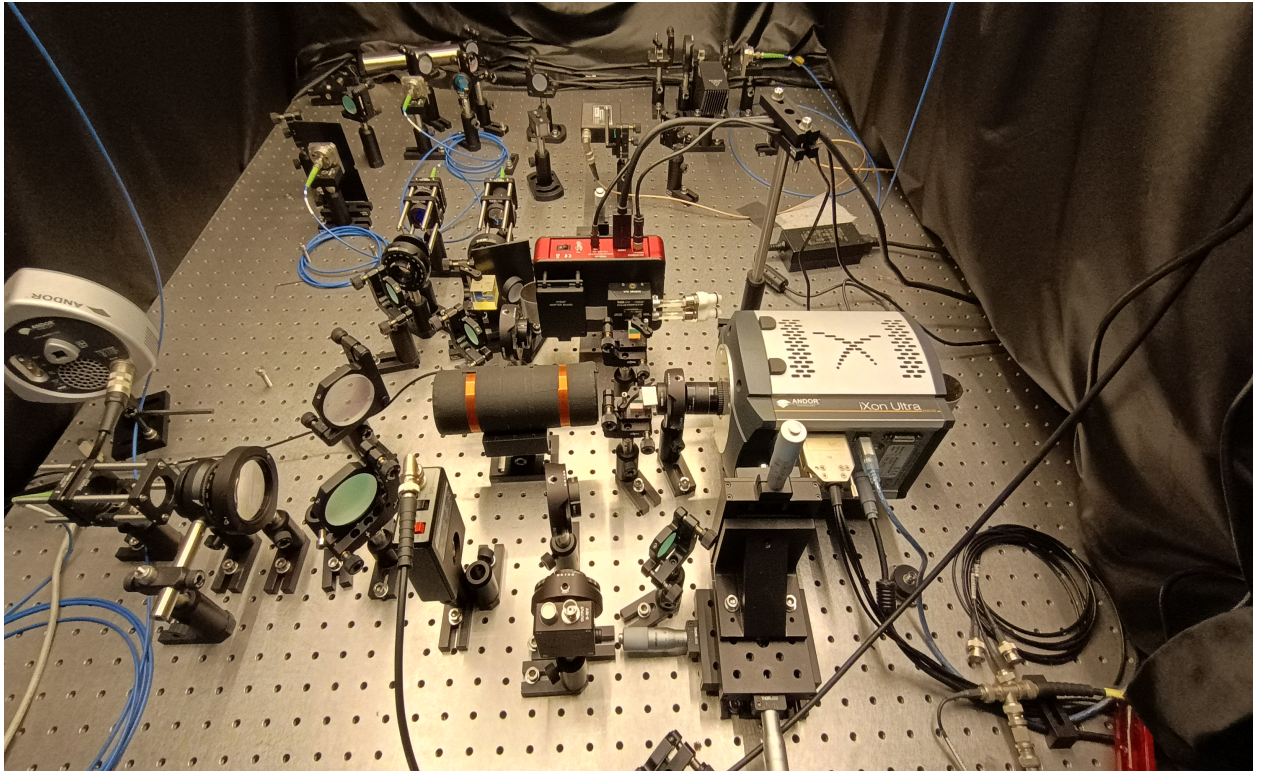


**Figure 4.4:** Experimental setup of a sub-tomographic imaging experiment

Absorption coefficient  $\alpha^+(x, y, \delta\nu)$  for  $\hat{\sigma}^+$  polarized component of imaging laser beam is a convolution of atomic population difference and absorption cross-section for a corresponding transition of an atom, which is given by

$$\alpha^+(x, y, \delta\nu) = \int_{-\infty}^{+\infty} \frac{\left[ n_1(x, y, v_z) - n_2^+(x, y, v_z) \right] \sigma_0^+(\frac{\Gamma^2}{4}) dv_z}{\left[ (2\pi\delta\nu - kv_z) + \frac{\Gamma^2}{4} \right]} \quad (4.9)$$

where  $\sigma_0^+$  is the peak absorption cross-section of  $\sigma^+$  atomic transition. Similarly, absorption coefficient  $\alpha^-(x, y, \delta\nu)$  for  $\hat{\sigma}^-$  polarized component of imaging laser beam is given by

$$\alpha^-(x, y, \delta\nu) = \int_{-\infty}^{+\infty} \frac{\left[ n_1(x, y, v_z) - n_2^-(x, y, v_z) \right] \sigma_0^-(\frac{\Gamma^2}{4}) dv_z}{\left[ (2\pi\delta\nu - kv_z) + \frac{\Gamma^2}{4} \right]} \quad (4.10)$$

where  $\sigma_0^-$  is the peak absorption cross-section of  $\sigma^-$  atomic transition. The absorption coefficient is reduced due to the saturation of absorption when imprinting and imaging laser beams interact with same velocity class. A decrease in absorption is different for  $\hat{\sigma}^+$  and  $\hat{\sigma}^-$  polarized components of imaging laser beam at different transverse locations. As a consequence of Kramers-Kronig relations, a change in absorption leads to a change in refractive index for each polarization component at different transverse locations, which is given by

$$\Delta\eta^\pm(x, y, \delta\nu) = -\Delta\alpha^\pm(x, y, \delta\nu)\delta\nu c/2v_r\Gamma \quad (4.11)$$

Consider  $\eta^+(x, y, \delta\nu)$  and  $\eta^-(x, y, \delta\nu)$  are the refractive indices of  $\hat{\sigma}^+$  and  $\hat{\sigma}^-$  polarization components of the imaging laser beam. For length  $L$  of the glass cell, the electric field of imaging laser beam at the entrance of glass cell is given by

$$E_{or} e^{-i(2\pi\nu_r t - kz)} \hat{y} \quad (4.12)$$

with an amplitude  $E_{or}$ . Therefore, electric field of the imaging laser beam after propagation through the atomic medium is given by

$$\vec{E}_r(x, y, \delta\nu) = \frac{E_{or} e^{-i2\pi\nu_r t} \left[ e^{-\alpha^+(x, y, \delta\nu)L} e^{i\eta^+(x, y, \delta\nu)kL} \hat{\sigma}^+ - e^{-\alpha^-(x, y, \delta\nu)L} e^{i\eta^-(x, y, \delta\nu)kL} \hat{\sigma}^- \right]}{i\sqrt{2}} \quad (4.13)$$

Consequently, the transmitted imaging laser beam becomes elliptically polarized. However, for  $\alpha^+(x, y, \delta\nu) \approx \alpha^-(x, y, \delta\nu)$ , atomic medium becomes circularly birefringent. Therefore, the transmitted electric field of imaging laser beam is written as

$$\vec{E}_r(x, y, \delta\nu) = \frac{E_{or} e^{-i2\pi\nu_r t} e^{-\alpha(x, y, \delta\nu)L} e^{i\eta^+(x, y, \delta\nu)kL} \left( \hat{\sigma}^+ - e^{i[\eta^-(x, y, \delta\nu) - \eta^+(x, y, \delta\nu)]kL} \hat{\sigma}^- \right)}{i\sqrt{2}} \quad (4.14)$$

where  $\alpha(x, y, \delta\nu) = \alpha^+(x, y, \delta\nu) \approx \alpha^-(x, y, \delta\nu)$ . As a result, the transmitted imaging laser beam exhibits a position and detuning dependent rotation of its plane of polarization. This

rotation is opposite for  $\phi(x, y) = +\pi/2$  and  $\phi(x, y) = -\pi/2$  at a given detuning  $\delta\nu$  and therefore, at a  $p_z = 2\pi m\delta\nu/k$ . Since this rotation depends on a transverse location on the beam wavefront, therefore an image is formed by passing the beam through an analyzing polarizer  $P_3$  with its pass axis oriented at an angle  $-45^\circ$  *w.r.t.*  $x$ -axis and by detecting its transverse intensity profile by an imaging camera-1. The intensity profile is evaluated and given by

$$I_r(x, y, \delta\nu) = \frac{I_{or} \left( 1 - \sin \left( \left[ \eta^+(x, y, \delta\nu) - \eta^-(x, y, \delta\nu) \right] kL \right) \right)}{2} \quad (4.15)$$

where  $I_{or} = c\epsilon_0 |E_{or}|^2 e^{-2\alpha(x, y, \delta\nu)L}/2$ ,  $c$  is the speed of light in vacuum and  $\epsilon_0$  is the vacuum permittivity. This intensity profile represents a  $2D$  section transverse to the  $p_z$ -axis of the  $3D$  localized phase space pattern. This sectional image at a detuning  $\delta\nu$  is a sub-tomograph around  $p_z = 0$ .

## 4.5 Experimental Method and Results

The experimental setup in the lab for the sub-tomographic imaging is shown in Figure 4.4. Experiment is conducted with gaseous  $^{87}\text{Rb}$  atoms filled in a glass cell of length  $L = 10$  cm, which is shielded from an external magnetic field. A uniform magnetic field  $\sim 0.25$  G is applied along  $z$ -axis. Main experimental schematic is shown in Figure 4.3. Imprinting laser light is produced by a single mode extended cavity diode laser of linewidth 1 MHz and its frequency is locked to the  $D_2$  transition of  $^{87}\text{Rb}$  atoms with a hyperfine ground state  $|F_g = 2\rangle$  and an excited state  $|F_g = 3\rangle$  at  $\lambda = 780$  nm. Imprinting laser light is passed through a single mode optical fiber to obtain a broad gaussian beam, which is collimated by a collimator. In Figure 4.3, the imprinting laser beam is first incident on  $SLM$  and a retro-reflected beam is further reflected by a polarization independent beam splitter  $BS-2$  into a glass cell filled with atomic gas. The material's optic axis lies in a plane perpendicular to the direction of propagation of light. If optic axis is parallel to direction of propagation of light, it will experience reduced birefringence. After reflection by  $BS-2$ , the birefringent phase pattern is denoted by  $\phi(x, y)$ . However, a transmitted part of the imprinting laser beam by  $BS-2$  is imaged by a camera-2 without any lens, which captures a direct intensity image as shown in Figure 4.2 (b). It can be seen that no image is formed on the camera. This transparent birefringent phase pattern is not visible however, only edges appear in the image due to diffraction at phase boundaries of transmitted beam

as the image is captured at a distance of 45 cm from the pattern. Light transmitted by a beam splitter  $BS-1$  is absorbed by a beam dumper to avoid any scattering into the camera. The plane of polarization of light incident on  $SLM$  is oriented at an angle  $-45^\circ$  *w.r.t.* a horizontal axis ( $z$ -axis) and this is achieved by rotating polarizer  $P_1$ . This beam propagating along  $-z$ -axis in the atomic medium is named as imprinting laser beam. Its polarization is transverse position dependent according to the pattern displayed on  $SLM$ . Imaging laser light is produced by a different single mode extended cavity diode laser of linewidth 1 MHz, which is locked to the same transition but its frequency can be shifted by the acoustic-optic modulators. Imaging laser light is passed through a single mode optical fiber to obtain a broad collimated gaussian beam. This collimated imaging beam is horizontally polarized along  $y$ -axis by a polarizer  $P_2$ . The polarized beam propagating along  $z$ -axis is overlapped with the imprinting laser beam in the glass cell. Intensity of imaging laser beam is  $\sim 90 \mu\text{W}/\text{cm}^2$  and of imprinting laser beam is  $\sim 1.2 \text{mW}/\text{cm}^2$ .

In this experiment, it is essential to measure a precise frequency difference between two laser beams, which is measured by shifting frequency of an extracted imprinting laser light by  $-110$  MHz and overlapping it with another extracted imaging laser light on a fast response photodetector  $D_2$  as shown in Figure 4.3 (b). These two laser beams interfere in time domain with beat frequency equals to a difference of laser frequencies. Frequency of a laser beat signal is measured by a radio frequency spectrum analyzer and detuning of imaging laser is evaluated. Rotation of a plane of polarization of imaging laser beam, after its propagation through the atomic medium, is analyzed by a polarizer  $P_3$  and its transverse intensity profile is captured by an EMCCD imaging camera-1 to construct sub-tomographic image.

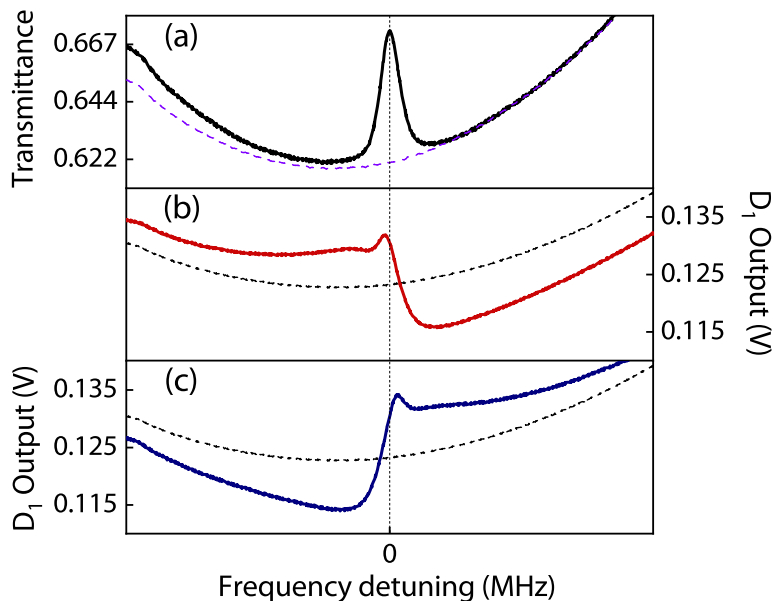


**Figure 4.5:** (a) Transmittance of atomic medium when both laser beams are linearly polarized. (b) Photodetector  $D_1$  output voltage when imprinting laser beam is  $\hat{\sigma}^+$  polarized. (c) when imprinting laser beam is  $\hat{\sigma}^-$  polarized. Dotted line represents the same plot without imprinting laser beam. Imaging laser beam is linearly polarized in all plots.

A part of the imaging laser beam is reflected by  $BS-3$  and a mirror onto a large area photodetector  $D_1$  after passing it through an analyzing polarizer  $P_4$  with its pass-axis oriented at an angle  $-45^\circ$  w.r.t.  $x$ -axis. This additional arrangement is used to obtain a frequency response of the atomic medium prior to the tomographic imaging experiment as shown in Figure 4.5. Where Figure 4.5 (a) represents a transmittance of the atomic medium when imaging and imprinting laser beams are linearly polarized and no pattern is displayed on  $SLM$ . An increase in transmittance is due to saturation of absorption caused by the imprinting laser beam. However, in contrast to an experiment described in Ref [1], where transmittance is important to construct a tomograph, in the present experiment the transmittance variation is not critically important. The detuning of imaging laser beam is measured w.r.t the peak of transmittance.

In Figure 4.5 (b), a  $\hat{\sigma}^+$  polarized imprinting laser beam is passed through the atomic medium, which produces a rotation of the plane of polarization of the imaging laser beam,

which is measured by  $P_4$  and photodetector  $D_1$  at different detuning  $\delta\nu$ . In Figure 4.5 (c), a  $\hat{\sigma}^-$  polarized imprinting laser beam is passed through the atomic medium, which produces an opposite rotation of the plane of polarization of imaging laser beam. A dotted line in plots of Figure 4.5 (a), (b) and (c) is the medium response when only imaging laser beam is passed through it and imprinting laser beam is blocked. In Figure 4.5 (a), imaging laser power is twenty percent higher than other plots. This experiment signifies the effect of imprinting laser beam. Therefore, atomic medium shows detectable response for different circular polarizations. After this measurement, a sub-tomographic imaging experiment is performed.

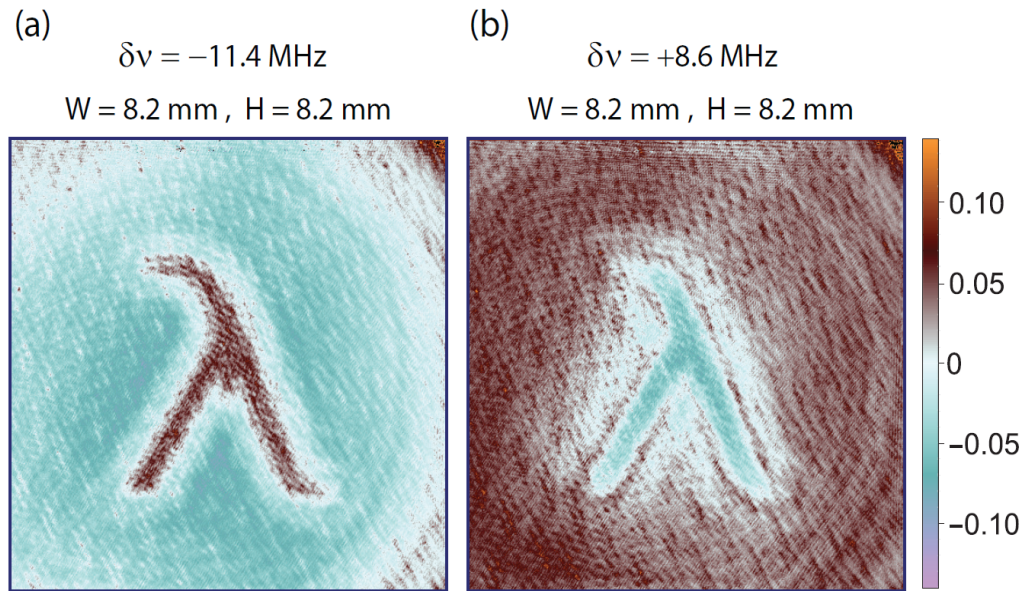


**Figure 4.6:** Two sub-tomographs of a 3D phase space localized pattern. Each plot is an experimentally constructed image,  $p(x, y, \delta\nu) = -\ln\left(\frac{I_r(x, y, \delta\nu)}{I_i(x, y, \delta\nu)}\right)$ . (a) For  $\delta\nu = -11.4 \text{ MHz}$ . (b) An inverted image for  $\delta\nu = +8.6 \text{ MHz}$ .

Experiment is controlled by a Lab-View program. A 3D position space localized pattern is displayed on SLM. To obtain a sub-tomographic image of a 3D phase space localized pattern, four different images are acquired for 200 m sec time of exposure on EMCCD imaging camera 1, where each images is separated by a time interval of 700 m sec from an adjacent images. First image is discarded and it is captured to clear the noise accumulated on EMCCD camera. A second image is captured in presence of imaging laser beam, in absence of imprinting laser beam and is denoted by  $I_i(x, y, \delta\nu)$ . A third image is captured in presence of imaging and imprinting laser beams, it corresponds to the image field and

denoted by  $I_m(x, y, \delta\nu)$ . A fourth image denoted by  $I_f(x, y)$  is captured in absence of imaging laser beam and in presence of imprinting laser beam. This images captures only the scattered light of imprinting laser beam. A background corrected image field is given by  $I_r(x, y, \delta\nu) = I_m(x, y, \delta\nu) - I_f(x, y)$ . A final sub-tomographic image at a detuning  $\delta\nu$  is constructed and given by  $p(x, y, \delta\nu) = -\ln\left(\frac{I_r(x, y, \delta\nu)}{I_i(x, y, \delta\nu)}\right)$ . Therefore,  $p(x, y, \delta\nu)$  is positive if a plane of polarization is rotated away from the pass-axis of polarizer  $P_3$  and negative if a plane of polarization is rotated towards the pass-axis, which is also evident from Figure 4.5. Two experimentally constructed sub-tomographic 2D images are shown in Figure 4.6, where (a) corresponds to a transverse section at  $\delta\nu = -11.4$  MHz and (b) corresponds to a transverse section at  $\delta\nu = +8.6$  MHz. These two sub-tomographic images are inverted *w.r.t.* each other.

## 4.6 Conclusion

This is the first experiment performed to image transparent birefringent phase pattern localized in phase space. It is an extension of an experiment described in Ref [1]. The experiment in Ref [1] can imprint and image only light absorbing objects. However, experiment conducted for the thesis can image objects which donot absorb light but exhibit polarization dependent phase shift of the transmitted light. Therefore, these phase space localized objects can modify the polarization of the transmitted light without absorption. The imprinting and tomographic imaging of such polarization-sensitive transparent pattern is the motivation behind the concept and experiment presented in the thesis. The present experiment is different from the Ref [1] experiment for the light absorbing pattern.

In the work described in this chapter, a transparent birefringent phase pattern was imrinted and imaged onto a phase space of an atomic gaseous medium by using atomic state dependent velocity selective hole burning. The transparent birefringent phase pattern changed the phase of transmitted light depending on the polarization and position of incident light. An imaging laser interacted with a position localized transparent birefringent phase pattern and is passed through a Doppler broadened atomic gaseous medium to imprint the pattern onto a phase space of atoms at room temperature. This pattern was imaged using a counter-propagating imaging laser beam of variable frequency. After imaging beam's polarization analysis, it was detected by a camera to construct two sub-tomographs of the imprinted phase space localized pattern. The two sub-tomographs obtained in this experiment were inverted *w.r.t.* each other. These two sub-tomographs

---

are separated by 20 MHz. This experiment can find applications where different position space transparent images can be selectively labeled by the momentum of atoms in phase-space. These different images can be reconstructed tomographically from the phase-space at different frequency of the imaging laser beam. From a direct application perspective, a real advantage of this type of image reconstruction is the extremely narrow frequency selectivity offered by the atomic medium, which corresponds to few tens of MHz. This is an extremely narrow optical multi-bandpass image filter. However, the main focus of this experiment is on the foundational significance of the concept introduced and its experimental feasibility.



# Chapter 5

## Conclusion

In this thesis, a novel concept and experiment of phase-space localized patterns and their tomographic imaging introduced by Mandip Singh in Ref [1] is discussed. The experiment is conducted with Rubidium atoms at room temperature. The thesis began with understanding the fine and hyperfine splitting in energy levels of  $^{87}\text{Rb}$  and  $^{85}\text{Rb}$ . Fine structure splitting due to the coupling of electron's spin magnetic moment with the magnetic field of proton was explained. These fine energy levels are further split into hyperfine energy levels. This hyperfine splitting in energy levels of electronic state is due to the interaction of electromagnetic field produced by the electrons at the nucleus with the electromagnetic multipole moments possessed by the nucleus. These hyperfine energy levels are not resolved due to Doppler broadening. The saturation absorption spectroscopy experiment was performed to resolve these hyperfine energy levels. In saturated absorption spectroscopy, two counterpropagating pump and probe beams were allowed to pass through the atomic vapor. The absorption of pump beam increased when it matches the resonant transition frequency of an atom, thereby increasing the transmission of probe beam. This change in absorption of probe beam generated signals in saturated absorption spectroscopy. Another experiment i.e. polarization doppler free spectroscopy was also performed. In polarization spectroscopy, the pump wave causes a change in the absorption coefficient  $\alpha$  as well as a change in refractive index  $n$ . The signals in the latter arised due to the change in the probe light polarization state induced by a polarized pump wave. The signals for laser frequency locking was generated using the setup of polarization spectroscopy.

The understanding of the atomic structure of Rubidium atoms provided a motivation for phase space imaging experiment. It is known that in conventional imaging exper-

iments, optically responsive objects in position space can be imaged using a lens and hence viewed by the human eye. The work described in this thesis goes beyond this usual imaging in position space and explained the concept of imaging phase space patterns. The pattern in phase space cannot be imaged with a lens conventionally and cannot be seen by the human eye. It is discussed how a stationary structural pattern can be created from object transparencies and imprinted onto the phase space of an atomic gaseous medium at room temperature. The experiment is based on the concept of velocity selective hole burning in the Doppler broadened absorption profile of an atomic gaseous medium. In contrast to previous work described in Ref [1], the current research is focussed on transparent phase-space localized patterns. The theory behind the imprinting and imaging of a transparent birefringent pattern in phase space of rubidium atoms is explained. Such a transparent birefringent phase pattern changes the phase of transmitted light, which depends on polarization and position of incident light without absorption. An experiment was conducted to imprint the birefringent phase pattern onto a phase space of an atomic gaseous medium by using atomic state dependent velocity selective hole burning. A laser beam of constant frequency, after interaction with a position space localized transparent birefringent phase pattern, is passed through a Doppler broadened atomic gaseous medium to imprint the pattern onto a phase space of atoms at room temperature. The pattern is localized in a unique three dimensional subspace of a six-dimensional phase space of atoms. A linearly polarized counter-propagating and overlapping imaging laser beam of variable frequency is detected by a camera after its polarization analysis to construct two sub-tomographs of the imprinted phase space localized pattern.

# Bibliography

- [1] Mandip Singh and Samridhi Gambhir. Three-dimensional classical imaging of a pattern localized in a phase space. *Physical Review A*, 98(5):053828, 2018. v, ix, x, 11, 12, 13, 43, 47, 48, 49, 50, 52, 53, 54, 66, 68, 71, 72
- [2] C. Wieman and T. W. Hänsch. Doppler-free laser polarization spectroscopy. *Phys. Rev. Lett.*, 36:1170–1173, May 1976. ix, 4, 5, 12, 17, 33
- [3] W. R. Bennett. Hole burning effects in a he-ne optical maser. *Phys. Rev.*, 126:580–593, Apr 1962. 1, 2, 13, 14, 46
- [4] Willis E. Lamb. Theory of an optical maser. *Phys. Rev.*, 134:A1429–A1450, Jun 1964. 1, 2, 13
- [5] Wolfgang Demtröder. *Laser spectroscopy*, volume 2. Springer, 1982. 1, 12, 17, 26, 27, 32, 33, 34, 46
- [6] Paul H Lee and Michael L Skolnick. Saturated neon absorption inside a 6238-Å laser. *Applied Physics Letters*, 10(11):303–305, 1967. 1, 2
- [7] A. Javan, E. A. Ballik, and W. L. Bond. Frequency characteristics of a continuous-wave he-ne optical maser. *J. Opt. Soc. Am.*, 52(1):96–98, Jan 1962. 1
- [8] A. Javan, W. R. Bennett, and D. R. Herriott. Population inversion and continuous optical maser oscillation in a gas discharge containing a he-ne mixture. *Phys. Rev. Lett.*, 6:106–110, Feb 1961. 1
- [9] Helen K Holt. Theory of gas lasers and its application to an experiment. *Physical Review A*, 2(1):233, 1970. 2
- [10] Stig Stenholm and Willis E Lamb Jr. Semiclassical theory of a high-intensity laser. *Physical Review*, 181(2):618, 1969. 2

- [11] Vladimir Georgievich Minogin and Vladilen Stepanovich Letokhov. *Laser light pressure on atoms*. CRC Press, 1987. 2
- [12] Harold J Metcalf and Peter Van der Straten. *Laser cooling and trapping*. Springer Science & Business Media, 1999. 2
- [13] Laser Cooling. Trapping of atoms. *J. Opt. Soc. Am. B*, 6:2020, 1989. 2
- [14] Richard G Brewer, MJ Kelly, and A Javan. Precision infrared stark spectra of n 14 h 2 d using lamb dip. *Physical Review Letters*, 23(11):559, 1969. 2
- [15] Th W Hänsch, MD Levenson, and AL Schawlow. Complete hyperfine structure of a molecular iodine line. *Physical Review Letters*, 26(16):946, 1971. 2
- [16] RL Barger and JL Hall. Pressure shift and broadening of methane line at 3.39  $\mu$  studied by laser-saturated molecular absorption. *Physical Review Letters*, 22(1):4, 1969. 2
- [17] Serge Haroche and Francis Hartmann. Theory of saturated-absorption line shapes. *Phys. Rev. A*, 6:1280–1300, Oct 1972. 3, 12, 44, 46, 48
- [18] CS Adams and E Riis. Laser cooling and trapping of neutral atoms. *Progress in quantum electronics*, 21(1):1–79, 1997. 3
- [19] Steven Chu. The manipulation of neutral particles. *Rev. Mod. Phys*, 70(3):685, 1998. 3, 4
- [20] Claude N Cohen-Tannoudji. Nobel lecture: Manipulating atoms with photons. *Reviews of Modern Physics*, 70(3):707, 1998. 3, 4
- [21] William D Phillips. Nobel lecture: Laser cooling and trapping of neutral atoms. *Reviews of Modern Physics*, 70(3):721, 1998. 3, 4
- [22] Ennio Arimondo. V coherent population trapping in laser spectroscopy. In *Progress in optics*, volume 35, pages 257–354. Elsevier, 1996. 3
- [23] Peter DD Schwindt, Svenja Knappe, Vishal Shah, Leo Hollberg, John Kitching, Li-Anne Liew, and John Moreland. Chip-scale atomic magnetometer. *Applied Physics Letters*, 85(26):6409–6411, 2004. 3

- 
- [24] Peter W Milonni. Controlling the speed of light pulses. *Journal of Physics B: Atomic, Molecular and Optical Physics*, 35(6):R31, 2002. 3
- [25] RW Boyd and DJ Gauthier. Progress in optics 43. page ch. 6, 2002. 3
- [26] Michael Fleischhauer, Atac Imamoglu, and Jonathan P Marangos. Electromagnetically induced transparency: Optics in coherent media. *Reviews of modern physics*, 77(2):633, 2005. 3
- [27] A Corney. Atomic and laser spectroscopy clarendon, 1977. 3
- [28] Demtroder Wolfgang. *Laser Spectroscopy: Basic Concepts and Instrumentation: 2nd Corrected Printing*. Springer-Verlag, 1982. 3, 35
- [29] Alan C Eckbreth. *Laser diagnostics for combustion temperature and species*, volume 3. CRC press, 1996. 4, 6
- [30] KB MacAdam, A Steinbach, and Carl Wieman. A narrow-band tunable diode laser system with grating feedback, and a saturated absorption spectrometer for cs and rb. *American Journal of Physics*, 60(12):1098–1111, 1992. 4, 32
- [31] LP Maguire, RMW Van Bijnen, E Mese, and RE Scholten. Theoretical calculation of saturated absorption spectra for multi-level atoms. *Journal of Physics B: Atomic, Molecular and Optical Physics*, 39(12):2709, 2006. 4, 12
- [32] William Happer. Light propagation and light shifts in optical pumping experiments. *Progress in quantum electronics*, 1:51–103, 1970. 4
- [33] RE Teets, FV Kowalski, WT Hill, N Carlson, and TW Hansch. Laser polarization spectroscopy. In *Advances in Laser Spectroscopy I*, volume 113, pages 80–87. SPIE, 1977. 5
- [34] Shigeru Nakayama. Optical pumping effects in high resolution laser spectroscopy. *Physica Scripta*, 1997(T70):64, 1997. 6
- [35] Shigeru Nakayama. Theoretical analysis of rb and cs d2 lines in doppler-free spectroscopic techniques with optical pumping. *Japanese journal of applied physics*, 24(1R):1, 1985. 6

- [36] ML Harris, CS Adams, SL Cornish, IC McLeod, E Tarleton, and IG Hughes. Polarization spectroscopy in rubidium and cesium. *Physical Review A*, 73(6):062509, 2006. 6, 12, 33, 34
- [37] Huy Diep Do, Geol Moon, and Heung-Ryoul Noh. Polarization spectroscopy of rubidium atoms: theory and experiment. *Physical Review A*, 77(3):032513, 2008. 6, 12, 36
- [38] Jung Bog Kim, Hong Jin Kong, and Sang Soo Lee. Dye laser frequency locking to the hyperfine structure ( $3s\ 1/2, f=2-3p\ 1/2, f=2$ ) of sodium d 1 line by using polarization spectroscopy. *Applied physics letters*, 52(6):417–419, 1988. 6
- [39] GPT Lancaster, RS Conroy, MA Clifford, J Arlt, and K Dholakia. A polarisation spectrometer locked diode laser for trapping cold atoms. *Optics communications*, 170(1-3):79–84, 1999. 6
- [40] CP Pearman, CS Adams, SG Cox, PF Griffin, DA Smith, and IG Hughes. Polarization spectroscopy of a closed atomic transition: applications to laser frequency locking. *Journal of Physics B: Atomic, Molecular and Optical Physics*, 35(24):5141, 2002. 6, 12, 41
- [41] Yutaka Yoshikawa, Takeshi Umeki, Takuro Mukae, Yoshio Torii, and Takahiro Kuga. Frequency stabilization of a laser diode with use of light-induced birefringence in an atomic vapor. *Applied optics*, 42(33):6645–6649, 2003. 6
- [42] A Ratnapala, CJ Vale, AG White, MD Harvey, NR Heckenberg, and H Rubinsztein-Dunlop. Laser frequency locking by direct measurement of detuning. *Optics letters*, 29(23):2704–2706, 2004. 6
- [43] VB Tiwari, S Singh, SR Mishra, HS Rawat, and SC Mehendale. Laser frequency stabilization using doppler-free bi-polarization spectroscopy. *Optics communications*, 263(2):249–255, 2006. 6
- [44] Karsten Danzmann, K Grützmacher, and B Wende. Doppler-free two-photon polarization-spectroscopic measurement of the stark-broadened profile of the hydrogen  $1\ \alpha$  line in a dense plasma. *Physical review letters*, 57(17):2151, 1986. 6
- [45] Po F Liao and GC Bjorklund. Polarization rotation induced by resonant two-photon dispersion. *Physical Review Letters*, 36(11):584, 1976. 6

- 
- [46] D Heiman, RW Hellwarth, MD Levenson, and Graham Martin. Raman-induced kerr effect. *Physical Review Letters*, 36(4):189, 1976. 6
- [47] BEA Saleih and MC Teich. Fundamental of photonics, 1991. 6
- [48] Frits Zernike. Phase contrast, a new method for the microscopic observation of transparent objects. *Physica*, 9(7):686–698, 1942. 7, 55
- [49] Frits Zernike. Phase contrast, a new method for the microscopic observation of transparent objects part ii. *Physica*, 9(10):974–986, 1942. 7, 55
- [50] Frits Zernike. How i discovered phase contrast. *Science*, 121(3141):345–349, 1955. 7, 55
- [51] SW Wilkins, T Ei Gureyev, D Gao, A Pogany, and AW Stevenson. Phase-contrast imaging using polychromatic hard x-rays. *Nature*, 384(6607):335–338, 1996. 7, 55
- [52] Timothy J Davis, D Gao, TE Gureyev, AW Stevenson, and SW Wilkins. Phase-contrast imaging of weakly absorbing materials using hard x-rays. *Nature*, 373(6515):595–598, 1995. 7
- [53] Ayman F Abouraddy, Patrick R Stone, Alexander V Sergienko, Bahaa EA Saleh, and Malvin C Teich. Entangled-photon imaging of a pure phase object. *Physical review letters*, 93(21):213903, 2004. 8
- [54] Shahaf Asban, Konstantin E Dorfman, and Shaul Mukamel. Quantum phase-sensitive diffraction and imaging using entangled photons. *Proceedings of the National Academy of Sciences*, 116(24):11673–11678, 2019. 8
- [55] Jeffrey H Shapiro. Computational ghost imaging. *Physical Review A*, 78(6):061802, 2008. 8
- [56] Yaron Bromberg, Ori Katz, and Yaron Silberberg. Ghost imaging with a single detector. *Physical Review A*, 79(5):053840, 2009. 8
- [57] Alessandra Gatti, Enrico Brambilla, Morten Bache, and Luigi A Lugiato. Ghost imaging with thermal light: comparing entanglement and classical correlation. *Physical review letters*, 93(9):093602, 2004. 8
- [58] Manpreet Kaur and Mandip Singh. Quantum imaging of a polarisation sensitive phase pattern with hyper-entangled photons. *Scientific Reports*, 11(1):1–11, 2021. 8

- [59] Aditya Saxena, Manpreet Kaur, Vipin Devrari, and Mandip Singh. Quantum ghost imaging of a transparent polarisation sensitive phase pattern. *Scientific Reports*, 12(1):1–9, 2022. 8
- [60] MR Andrews, M-O Mewes, NJ Van Druten, DS Durfee, DM Kurn, and W Ketterle. Direct, nondestructive observation of a bose condensate. *science*, 273(5271):84–87, 1996. 9
- [61] JM Higbie, LE Sadler, S Inouye, AP Chikkatur, SR Leslie, KL Moore, V Savalli, and DM Stamper-Kurn. Direct nondestructive imaging of magnetization in a spin-1 bose-einstein gas. *Physical review letters*, 95(5):050401, 2005. 9
- [62] M Kohonen, PG Petrov, RA Nyman, and EA Hinds. Minimally destructive detection of magnetically trapped atoms using frequency-synthesized light. *New Journal of Physics*, 13(8):085006, 2011. 9
- [63] W Ketterle, DS Durfee, D Stamper-Kurn, M Inguscio, S Stringari, and CE Wieman. Bose-einstein condensation in atomic gases (proceedings of the international school of physics). *Enrico Fermi”, course CXL,”(IOS Press, 1999) Chap. Making, probing and understanding Bose-Einstein condensates*, pages 67–176, 1999. 9
- [64] Miroslav Gajdacz, Poul L Pedersen, Troels Mørch, Andrew J Hilliard, Jan Arlt, and Jacob F Sherson. Non-destructive faraday imaging of dynamically controlled ultracold atoms. *Review of Scientific Instruments*, 84(8):083105, 2013. 9
- [65] Kendall B Davis, M-O Mewes, Michael R Andrews, Nicolaas J van Druten, Dallin S Durfee, DM Kurn, and Wolfgang Ketterle. Bose-einstein condensation in a gas of sodium atoms. *Physical review letters*, 75(22):3969, 1995. 10
- [66] Mike H Anderson, Jason R Ensher, Michael R Matthews, Carl E Wieman, and Eric A Cornell. Observation of bose-einstein condensation in a dilute atomic vapor. *science*, 269(5221):198–201, 1995. 10
- [67] Ayman F Abouraddy, Bahaa EA Saleh, Alexander V Sergienko, and Malvin C Teich. Role of entanglement in two-photon imaging. *Physical review letters*, 87(12):123602, 2001. 11
- [68] Ryan S Bennink, Sean J Bentley, and Robert W Boyd. “two-photon” coincidence imaging with a classical source. *Physical review letters*, 89(11):113601, 2002. 11

- 
- [69] Alejandra Valencia, Giuliano Scarcelli, Milena D'Angelo, and Yanhua Shih. Two-photon imaging with thermal light. *Physical review letters*, 94(6):063601, 2005. 11
- [70] Fabio Ferri, Davide Magatti, Alessandra Gatti, Morten Bache, Enrico Brambilla, and Luigi A Lugiato. High-resolution ghost image and ghost diffraction experiments with thermal light. *Physical review letters*, 94(18):183602, 2005. 11
- [71] Jeffrey H Shapiro, Dheera Venkatraman, and Franco NC Wong. Classical imaging with undetected photons. *Scientific Reports*, 5(1):1–8, 2015. 11
- [72] Daniel A Steck. Rubidium 87 d line data. 2001. 12, 24
- [73] Paul Siddons, Charles S Adams, Chang Ge, and Ifan G Hughes. Absolute absorption on rubidium d lines: comparison between theory and experiment. *Journal of Physics B: Atomic, Molecular and Optical Physics*, 41(15):155004, 2008. 12, 32
- [74] HD Do, MS Heo, G Moon, HR Noh, and W Jhe. Analytic calculation of the lineshapes in polarization spectroscopy of rubidium. *Optics communications*, 281(15-16):4042–4047, 2008. 12, 41
- [75] Stefan Putz, Andreas Angerer, Dmitry O Krimer, Ralph Glattauer, William J Munro, Stefan Rotter, Jörg Schmiedmayer, and Johannes Majer. Spectral hole burning and its application in microwave photonics. *Nature Photonics*, 11(1):36–39, 2017. 13, 14
- [76] Daryl W Preston. Doppler-free saturated absorption: Laser spectroscopy. *American Journal of Physics*, 64(11):1432–1436, 1996. 13, 22, 25, 28, 32
- [77] Nouredine Zettili. Quantum mechanics: concepts and applications, 2003. 18, 19
- [78] David J Griffiths and Darrell F Schroeter. *Introduction to quantum mechanics*. Cambridge university press, 2018. 18
- [79] Brian Harold Bransden and Charles Jean Joachain. *Physics of atoms and molecules*. Pearson Education India, 2003. 19, 20, 21
- [80] Wolfgang Demtröder. *Atoms, molecules and photons*, volume 3. Springer, 2010. 19, 25
- [81] David R Lide. *CRC handbook of chemistry and physics*, volume 85. CRC press, 2004. 23

- [82] Ennio Arimondo, M Inguscio, and P Violino. Experimental determinations of the hyperfine structure in the alkali atoms. *Reviews of Modern Physics*, 49(1):31, 1977. 23
- [83] Jörgen Gustafsson, Dorys Rojas, and Ove Axner. The influence of hyperfine structure and isotope shift on the detection of rb atoms in atmospheric pressure atomizers by the 2f-wavelength modulation technique. *Spectrochimica Acta Part B: Atomic Spectroscopy*, 52(13):1937–1953, 1997. 23
- [84] Umakant D Rapol, Anusha Krishna, and Vasant Natarajan. Precise measurement of hyperfine structure in the state of rb. *The European Physical Journal D-Atomic, Molecular, Optical and Plasma Physics*, 23:185–188, 2003. 23
- [85] Jun Ye, Steve Swartz, Peter Jungner, and John L Hall. Hyperfine structure and absolute frequency of the 87 rb 5p 3/2 state. *Optics letters*, 21(16):1280–1282, 1996. 24
- [86] U Volz and H Schmoranzer. Precision lifetime measurements on alkali atoms and on helium by beam–gas–laser spectroscopy. *Physica Scripta*, 1996(T65):48, 1996. 24
- [87] GP Barwood, P Gill, and WRC Rowley. Frequency measurements on optically narrowed rb-stabilised laser diodes at 780 nm and 795 nm. *Applied Physics B*, 53:142–147, 1991. 24
- [88] Nibedita Ram, M Pattabiraman, and C Vijayan. Low field zeeman magnetometry using rubidium absorption spectroscopy. In *Journal of Physics: Conference Series*, volume 80, page 012035. IOP Publishing, 2007. 24
- [89] BJ Feldman and MS Feld. Theory of a high-intensity gas laser. *Physical Review A*, 1(5):1375, 1970. 45
- [90] Th Hänsch and P Toschek. Theory of a three-level gas laser amplifier. *Zeitschrift für Physik A Hadrons and nuclei*, 236(3):213–244, 1970. 45